Experimental Mechanics
https://doi.org/10.1007/s11340-025-01164-3

RESEARCH PAPER

Extracting Mixed-Mode Fracture Parameters Using Two Vision-based Methods: Comparison of Combined Fields Method with Legacy Approach

A. Edwards[1] · J. Cho[1] · H. Tippur[1]

Received: 14 October 2024 / Accepted: 18 February 2025

Abstract

Background Over-deterministic least-squares methods of extracting SIFs from measured full-field quantities in conjunction with asymptotic fields has been the mainstay of experimental fracture mechanics. The vision-based methods of Digital Image Correlation (DIC) to determine displacements and Digital Gradient Sensing (DGS) to determine stress gradients have played an important role in this regard.

Objectives In DIC and DGS, two or more orthogonal fields are measured simultaneously. Yet, while extracting SIFs, often only one of the components is picked based on intuition/legacy. This could result in erroneous SIF values under mixed-mode conditions.

Methods Robustness of SIF extraction by utilizing all components in tandem is demonstrated over a wide range of pure- and mixed-mode conditions. An edge-notched semi-circular specimen geometry is used to create different mode-mixities. The data from DIC and DGS are processed using both the combined fields and legacy approaches. The accuracy and robustness of the former relative to the latter is demonstrated for (a) different number of higher order terms in the asymptotic series, (b) crack tip location uncertainty, and (c) different regions of data extraction.

Results An order of magnitude reduction in standard deviation and root-mean-squared error in mixed and pure mode SIFs are seen for DIC and the combined fields method. Marginal improvements are seen when the crack tip position or the region of interest are varied in DGS.

Conclusions Robustness of extracting mixed-mode SIFs accurately by employing all measured fields concurrently in an over-deterministic least-squares approach is superior to using a single component based on intuition/legacy.

Keywords Fracture mechanics · Stress intensity factors · Digital image correlation · Digital gradient sensing · Least-squares analysis

Nomenclatures

r	Radial coordinate
θ	Angular coordinate
u_x	x Displacement
u_y	y Displacement
ϕ_x	x Angular deflection
ϕ_y	y Angular deflection
C_σ	Stress optic constant
B	Thickness of the specimen
σ_x	Stress in the x direction
σ_y	Stress in the y direction
μ	Shear modulus
κ	Kolosov constant
n	Number of terms in the analysis
β	Crack Angle
S	Span Length
px	Pixel

Abbreviations

DIC	Digital Image Correlation
DGS	Digital Gradient Sensing
SCB	Semi Circular Beam
ROI	Region of Interest
CGS	Coherent Gradient Sensing
P	Load
a	Crack Length

H. Tippur is a member of SEM.

✉ H. Tippur
tippuhv@auburn.edu

[1] Department of Mechanical Engineering, Auburn University, Auburn, AL 36849, USA

Published online: 14 March 2025

R	Radius of specimen
δ	Distance between specimen and target
K_I	Mode-I stress intensity factor
K_{II}	Mode-II stress intensity factor
Y_I	Mode-I geometry factor
Y_{II}	Mode-II geometry factor
f_I	Function relating u_x to K_I
f_{II}	Function relating u_x to K_{II}
g_I	Function relating u_y to K_I
g_{II}	Function relating u_y to K_{II}
p_I	Function relating ϕ_x to K_I
p_{II}	Function relating ϕ_x to K_{II}
q_I	Function relating ϕ_y to K_I
q_{II}	Function relating ϕ_y to K_{II}
SIF	Stress Intensity Factor
LEFM	Linear Elastic Fracture Mechanics
PMMA	Poly(methyl methacrylate)
RMSE	Root Mean Square Error

Introduction

In many early experimental fracture mechanics studies, local measurements from strain gages or far-field measurements from a load-cell were often used to evaluate fracture parameters. With the advent of full-field optical methods (photoelasticity [1], Twyman-Green interferometry [2], moiré interferometry [3] and Coherent Gradient Sensing (CGS) [4]) over the past few decades, the mechanical fields measured directly near the crack tip were found to offer richer data sets for better fracture parameter evaluation as well as to discover new aspects of the fracture process itself. The full-field data from analog optical fringes also enabled improved fracture parameter extraction schemes based on over-deterministic least-squares error minimization when used in conjunction with analytical crack tip field descriptions [5]. In recent years, vision-based full-field digital techniques such as digital photoelasticity, Digital Image Correlation (DIC) [6], and Digital Gradient Sensing (DGS) [7], have become viable for making reliable crack tip field measurements. Furthermore, these have found adoption in experimental fracture mechanics studies since digital techniques offer simpler data extraction and processing steps when compared to their analog counterparts. In this context, the focus of the current work is to ascertain the improved accuracy and robustness of over-deterministic data analyses when multiple data sets are utilized concurrently instead of only a single component for parameter extraction [8–11] based on intuition, availability or legacy. Although this approach of utilizing fields concurrently has been found superior in case of mode-I problem [12–16], it is important to extend and evaluate it for a wide range of mixed-mode fracture conditions and for different optical methods yielding different mechanical quantities, for example DIC and DGS, for comparison while studying the same problem. In the literature, it is common for works using DIC [10, 17] and DGS [1, 7, 18] to only use one field although two or more are measured. The objective of this work is to adapt the combined fields method to DGS alongside DIC and evaluate its effectiveness for mixed-mode conditions. This would demonstrate the reliability of the approach when examining real world fracture events [19] which are often mixed-mode in nature. The two measurement methods, DIC and DGS, that measure different mechanical fields, namely displacements and stress gradients, from random speckle image correlation principle, allows for testing of the combined fields and legacy approaches on distinctly different fields.

Real-time interferometric methods such as moiré or CGS typically offer a single component of the mechanical field in the analog format as optical fringes at a load-step or a time instant when a traditional setup is used. Vision-based DIC and DGS techniques, on the other hand, produce multiple orthogonal field quantities simultaneously, though not in real-time. Each of these techniques requires a post-processing step that involves random speckle image correlation to determine the mechanical fields encoded in the captured images during deformation. The measurement accuracy in these is dependent on many factors including the camera resolution, size of the sub-images, image correlation algorithm, characteristics of the random pattern used, and overlap between neighboring sub-images, among others [20–22]. More importantly, vision-based techniques allow inclusion of more complete data sets for extracting fracture parameters such as stress intensity factors (SIFs) since characterization of brittle fracture relies heavily on accurate determination of critical SIFs at crack initiation and during growth. Since cracks generally propagate under mixed-mode conditions, the nature of crack tip loading or mode-mixity needs to be separated into individual modes by quantifying different SIFs correctly. Thus, using a single component of the complete data set could have intrinsic deficiencies in terms of accuracy of different SIFs. For example, Tippur et al. [23] have shown that in CGS, the accuracy of the mode-I SIF depended on (a) the component of the stress gradient field adopted for the analysis, (b) the sectors where the data for analysis came from, and (c) the number of higher order terms in the asymptotic expression used. Similarly, Yoneyama et al. [24] has shown that using radial displacement field u_r instead of the measured Cartesian components u_x or u_y alone leads to a more accurate mode-I SIF determination under quasi-static conditions. Kirugulige and Tippur [25] have subsequently shown this to be the true for inertial loading conditions as well. A different approach of obtaining accurate fracture parameters from DIC is to evaluate the path-independent J-integral values instead and then evaluate the individual SIFs via mode-partitioning [12, 26]

techniques. However, mode-partitioning would often need companion finite element analyses. In light of all these, accurate assessment of different SIFs in pure- and mixed-mode conditions by utilizing all available components of the mechanical fields is appealing.

In this work, edge-cracked Semi-Circular Beam (SCB) geometry with different crack angles is used to simulate a wide range of mode-mixities from pure mode-I to mode-II [27–29]. (Recently, there is also a report in the literature [30] studying mode-I/III cracks with a novel torsional geometry with spiral grooves). Two vision-based methods, namely DIC and DGS, are implemented for measuring two orthogonal displacement and stress gradient fields for different crack angles. Both the legacy and the new combined fields approaches are employed to extract SIFs from each optical method to study the accuracy and robustness based on the number of terms in the asymptotic fields, potential crack tip location errors and the region of interest where the data is extracted for analysis. Following this Introduction, the rationale for using SCB geometry is discussed in Sect. "Specimen Geometry", and brief descriptions of DIC and DGS approaches and their implementation are discussed in Sect. "Optical Methods". Subsequently, the legacy and combined fields approaches are described for both DIC and DGS in Sect. "Data Extraction Approaches". The experimental crack tip field measurements from DIC, the SIF results for different data analysis parameters are presented and discussed first in Sects. "Experimental Setup: DIC" and "Results and Discussion: DIC". This is followed in Sects. "Experimental Setup: DGS" and "Results and Discussion: DGS" by the crack tip field measurements from DGS, the SIF results and discussion for different data analysis parameters before drawing major conclusions of this work.

Specimen Geometry

Mixed-mode fracture conditions of different mode-mixities ranging from pure mode-I to pure mode-II are difficult to induce in a controlled fashion in a single edge-cracked specimen geometry. In the literature, there are examples of geometries and loading configurations commonly used to accomplish this task. For example, the edge-cracked four-point asymmetric beam geometry, centrally cracked Brazilian disk geometry, and edge or centrally cracked specimens tested using Arcan fixtures are designs where the specimen geometry remains the same, but the loading configuration is altered to achieve the desired mode-mixities. There are other designs where the loading configuration remains the same but the specimen geometry (e.g., crack angle) is altered between tests to achieve the full range of mode-mixites. In the latter category, a simple yet highly versatile edge cracked Semi-Circular Beam (SCB) geometry with a single crack tip has been popular; see, Fig. 1(a). It can be used for both quasi-static and dynamic brittle fracture studies. Chong and Kuruppu (1984) devised this geometry to allow a simple three-point bend loading of specimens obtained from cored geological or cementitious samples [28]. In the SCB geometry, wide ranging mixed-mode conditions can be achieved using a three-point bending configuration [29–32] and by only varying the angle the crack makes relative to the loading direction. The same geometry can be extended to dynamic conditions either in a one-point or three-point impact loading configuration [29] as well.

In this work, SCB specimens made of PMMA were used for creating the complete range of mixities from pure mode-I to mode-II. Using a laser cutter, specimens with different crack angles β were cut out of a single sheet of commercially purchased material, and then scored with a razorblade. The nature of these experiments is such that the cracks were loaded not to initiate (or grow) them but produce sufficient deformation to enable measurement and analysis within the LEFM bounds. Any heat effects due to laser cutting is negligible in the Region of Interest (ROI) utilized for analyses, which is expounded on in later sections. An important consideration when utilizing this geometry was that the loading

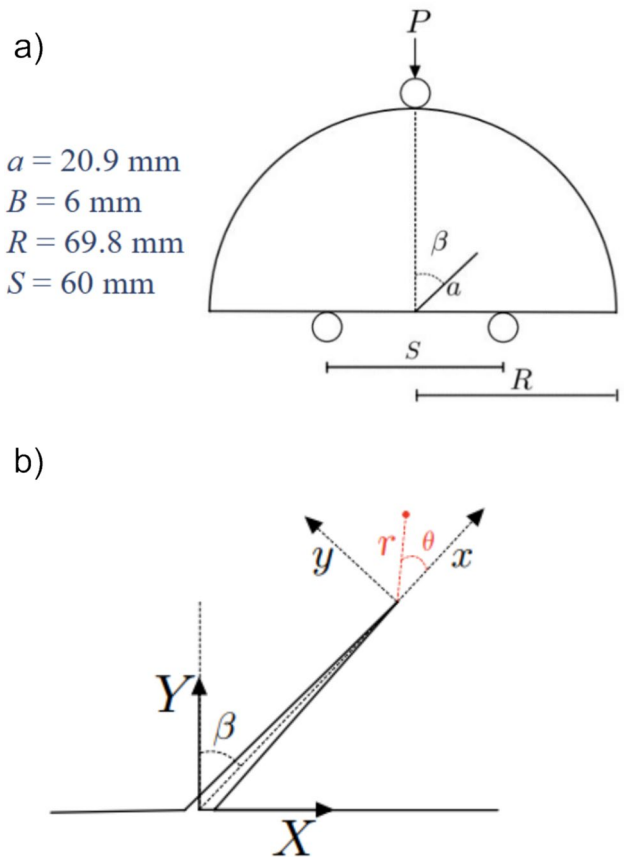

Fig. 1 **a** Semi-Circular Bend (SCB) specimen geometry. **b** The local and global coordinate systems adopted

pin had to be aligned carefully to avoid asymmetric loading from affecting the results. The mixed-mode SIFs for this geometry are expressed as [29],

$$K_I = Y_I \frac{P}{2RB}\sqrt{\pi a} \tag{1}$$

$$K_{II} = Y_{II} \frac{P}{2RB}\sqrt{\pi a} \tag{2}$$

where Y_I and Y_{II} are geometric factors. The previous investigators have used finite element analysis to evaluate Y_I and Y_{II} for different crack angles [29]. By utilizing their work, five crack angles were selected for experimentation and are listed in Table 1. These provide a theoretical baseline value of K_I and K_{II} to compare the legacy and the combined fields techniques.

In this work, a local Cartesian crack tip coordinate system (x, y) is defined such that the crack is oriented in the positive x-direction, see Fig. 1(b). A global coordinate system is also defined as the X- and Y-directions such that the load is applied in the negative Y-direction. Additionally, since the specimen thickness used is relatively small when compared to the planar dimensions, plane stress assumptions were adopted.

Optical Methods

Digital Image Correlation (DIC)

2D Digital Image Correlation (DIC) is an optical method that utilizes a random pattern of black and white speckles on a specimen surface (Fig. 2(a)) in order to evaluate the local displacements during a loading sequence. As the specimen deforms, speckle images are recorded at load-steps of 100 N to be compared with the one at a reference load. The recorded grayscale images are then segmented into sub-images or facets during the post-processing step. The size of the sub-images and the spacing between them is determined by a number of factors including the camera pixel resolution, size of the speckles, and the optical magnification (or the scale factor) used while recording. Upon performing image correlation, the location of the sub-images in the deformed state relative to their positions in the reference state are determined to obtain displacements in two orthogonal directions (say, x- and y-directions). The measured deformations are typically visualized at a load-step as a contour map, a color map or both. Due to the immense popularity of this method in recent years, further details are avoided here for brevity and can be found in many reports [33, 34] and monographs [6].

Table 1 Geometric factors for the selected crack angles

Crack Angle, β	Y_I	Y_{II}	Mode
0°	2.00	0.00	Mode-I
15°	1.75	0.55	Mixed Mode
30°	1.00	0.90	Mixed Mode
40°	0.45	0.85	Mixed Mode
50°	0.00	0.65	Mode-II

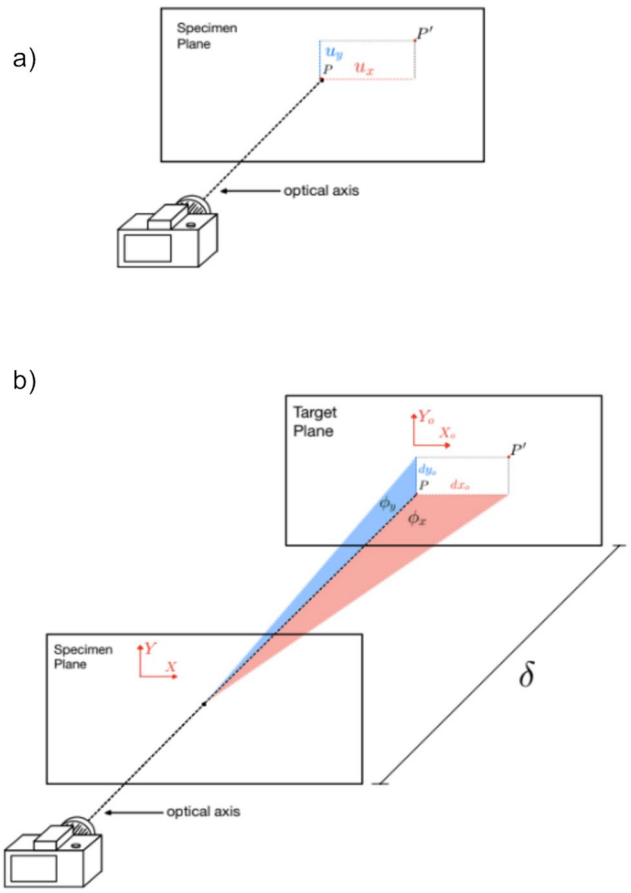

Fig. 2 Schematic for **a** measurement of displacements in DIC, **b** measurement of angular deflections in transmission-mode DGS

Digital Gradient Sensing (DGS)

Digital Gradient Sensing (DGS) is an optical technique that measures local angular deflections of light rays in two orthogonal planes. These physical quantities are proportional to two orthogonal stress gradients in the specimen. The method can be employed for studying both transparent (in transmission mode) and opaque materials (in reflection mode). The transmission mode was used in the current work due to the transparency of PMMA. Experimentally, DGS relies on correlation of speckle images in the deformed and reference states to assess the local elasto-optical effects experienced by the specimen.

The random speckle pattern in this method is on a planar target at a predetermined distance δ behind and parallel to the transparent specimen, and recorded through the specimen. As the specimen deforms, the perceived displacements of speckles on the target plane relative to the reference state due to the combined refractive index changes (stress-optic effect) and specimen thickness change (Poisson effect) are evaluated. The measured angular deflections from DGS are obtained as [7],

$$\phi_{x;y} = \tan^{-1}\left(\frac{dx_o;dy_o}{\delta}\right) \tag{3}$$

and are depicted in Fig. 2(b) where dx_o and dy_o denote the perceived speckle field shifts and δ denotes the gap between the specimen and speckle target planes used in an experiment.

By determining these angular deflections, the stress gradients in the material can be evaluated by knowing the stress-optic constant of the material and the nominal thickness of the specimen. The measured angular deflections are related to stress gradients as [7, 35, 36,]:

$$\phi_{x;y} = \pm C_\sigma B \frac{\partial(\sigma_x + \sigma_y)}{\partial(x;y)} \tag{4}$$

It is worth noting that, under the assumption of paraxiality, the angular deflections are related to points on the specimen and not the camera/image coordinates. Furthermore, the rigid specimen motions in DGS produce [35], within measurement errors, zero angular deflections across the ROI, and thus are ignored.

Data Extraction Approaches

As noted earlier, this work will compare two approaches of extracting SIF values from the same measured data set. These extraction approaches are applicable to both DIC and DGS methods. For DIC, extracting SIFs utilizes Williams' asymptotic expressions for in-plane displacement components [8]:

$$\begin{aligned} u_x = &\sum_{n=1}^{N} \frac{(K_I)_n r^{n/2}}{2\mu\sqrt{2\pi}}\left[\kappa\cos\frac{n\theta}{2} - \frac{n}{2}\cos\left(\frac{n}{2}-2\right)\theta + \left(\frac{n}{2}+(-1)^n\right)\cos\frac{n\theta}{2}\right] \\ &+ \sum_{n=1}^{N} \frac{(K_{II})_n r^{n/2}}{2\mu\sqrt{2\pi}}\left[\kappa\sin\frac{n\theta}{2} - \frac{n}{2}\sin\left(\frac{n}{2}-2\right)\theta + \left(\frac{n}{2}+(-1)^n\right)\sin\frac{n\theta}{2}\right] + P \end{aligned} \tag{5}$$

$$\begin{aligned} u_y = &\sum_{n=1}^{N} \frac{(K_I)_n r^{n/2}}{2\mu\sqrt{2\pi}}\left[\kappa\sin\frac{n\theta}{2} + \frac{n}{2}\sin\left(\frac{n}{2}-2\right)\theta - \left(\frac{n}{2}+(-1)^n\right)\sin\frac{n\theta}{2}\right] \\ &+ \sum_{n=1}^{N} \frac{(K_{II})_n r^{n/2}}{2\mu\sqrt{2\pi}}\left[-\kappa\cos\frac{n\theta}{2} - \frac{n}{2}\cos\left(\frac{n}{2}-2\right)\theta + \left(\frac{n}{2}+(-1)^n\right)\cos\frac{n\theta}{2}\right] + Q \end{aligned} \tag{6}$$

In the above, u_x and u_y are displacement components in the x- and y-directions, respectively, $(K_I)_n$ and $(K_{II})_n$ are the n^{th} mode-I and mode-II coefficients of the expansion, r and θ are the crack tip polar coordinates of the data points on the specimen (Fig. 1b), μ is the shear modulus, κ is the Kolosov constant defined as $(3-\nu)/(1+\nu)$ for plane stress where ν is the Poisson's ratio and P and Q denote rigid body motions. The coefficients associated with the leading term ($n=1$) are the mode-I and mode-II SIFs K_I and K_{II}, respectively. The higher order terms ($n>1$) and the associated coefficients describe the far-field effects due to the specimen geometry and loading configuration utilized. Successful extraction of accurate K_I and K_{II} is key to single-parameter LEFM-based analysis and design. It is worth noting that post-processing of speckle images in DIC results in a very large data set (of the order of 10^3–10^4) corresponding to different locations near the crack tip. Furthermore, each data point is affected by different amounts of far-field/boundary effects when finite specimen geometries and loading configurations are used. Therefore, to extract accurate values of SIFs using all the data in the ROI, an over-deterministic linear least-squares error minimization is performed. (Using small scale plastic zone size calculation, for the maximum observed K_I in the experiments, the radius of the plastic zone is $\sim 100\mu m$. As the ROI has a minimum diameter of 1.5 mm, these effects can be safely ignored.) For simplicity, let the Williams' asymptotic expressions in equations (5) and (6) can be rewritten as:

$$u_x = \sum_{n=1}^{N} f_{I_n}(r,\theta)(K_I)_n + f_{II_n}(r,\theta)(K_{II})_n + P \tag{7}$$

$$u_y = \sum_{n=1}^{N} g_{I_n}(r,\theta)(K_I)_n + g_{II_n}(r,\theta)(K_{II})_n + Q \tag{8}$$

Here, the functions $f(r,\theta)$ and $g(r,\theta)$ have subscripts I or II denoting that the function is multiplied by a mode-I or mode-II coefficient, respectively. The subscript n denotes the number of the term in the expansion from $n=1$ to N terms.

Similarly, for experiments using DGS, the relationship between angular deflections of light rays and SIFs are given by [36],

$$\phi_x = C_\sigma B\left[\left(\sum_{n=1}^{N}(K_I)_n\left(\frac{n}{2}-1\right)\sqrt{\frac{2}{\pi}}r^{\left(\frac{n}{2}-2\right)}\cos\left(\frac{n}{2}-2\right)\theta]\right)+\left(\sum_{n=1}^{N}(K_{II})_n\left(\frac{n}{2}-1\right)\sqrt{\frac{2}{\pi}}r^{\left(\frac{n}{2}-2\right)}\sin\left(\frac{n}{2}-2\right)\theta\right)\right] \quad (9)$$

$$\phi_y = -C_\sigma B\left[\left(\sum_{n=1}^{N}(K_I)_n\left(\frac{n}{2}-1\right)\sqrt{\frac{2}{\pi}}r^{\left(\frac{n}{2}-2\right)}\sin\left(\frac{n}{2}-2\right)\theta\right)-\left(\sum_{n=1}^{N}(K_{II})_n\left(\frac{n}{2}-1\right)\sqrt{\frac{2}{\pi}}r^{\left(\frac{n}{2}-2\right)}\cos\left(\frac{n}{2}-2\right)\theta\right)\right] \quad (10)$$

where ϕ_x and ϕ_y are the angular deflection in the x–z and y–z planes (where z is the optical axis, perpendicular to the specimen plane) respectively, $(K_I)_n$ and $(K_{II})_n$ are the coefficients of mode-I and mode-II expansion fields, r and θ are the local polar coordinates of the location of the data point on the specimen, C_σ is the elasto-optic constant of the material, and B is the specimen thickness. In the DGS field description, $(K_I)_n$ and $(K_{II})_n$ are again coefficients of the series, and the ones corresponding to $n=1$ are the SIFs K_I and K_{II}. Note that the $n=2$ terms in the expansion vanish, which is unlike the DIC counterpart, and $n=4$ terms are constants. Furthermore, the measured fields dominate the crack vicinity in DGS, also unlike DIC, due to the negative powers of r up to $n=3$. Much like in DIC, numerous data points for angular deflections are measured near the crack. Hence, individual data points are again affected by different amounts of far-field or boundary effects due to the finite specimen dimensions and geometry as well as the loading configuration. Therefore, an over-deterministic linear least-squares error minimization analysis can extract SIFs K_I and K_{II} from the data set reliably. Let the above equations be rewritten for simplicity as,

$$\phi_x = \sum_{n=1}^{N} p_{In}(r,\theta)(K_I)_n + p_{IIn}(r,\theta)(K_{II})_n \quad (11)$$

$$\phi_y = \sum_{n=1}^{N} q_{In}(r,\theta)(K_I)_n + q_{IIn}(r,\theta)(K_{II})_n \quad (12)$$

The functions $f(r,\theta)$, $g(r,\theta)$, $p(r,\theta)$, and $q(r,\theta)$ depend on polar coordinates r and θ with the origin centered at the crack tip. In both of these methods, the location of the crack tip is typically identified using the recorded images and/or the contour plots of the correlated data representing the measured field to define the local coordinate system.

Legacy Approach

The legacy approach of extracting SIFs involves a single component of the measured field even when multiple components are available. This practice is rooted in the fact that the analog methods such as moiré or CGS employing traditional setups typically yield only one component of the displacement or stress gradient fields instead of multiple orthogonal components as in the vision-based methods DIC and DGS. As a result, a mechanical field judged by the operator as suitable (say, u_y from moiré method for mode-I) is measured and used subsequently in an over-deterministic least-squares analysis for SIF extraction. Although this approach has generally produced satisfactory results for the dominant SIF (for example, K_I in mode-I dominant cases), the accuracy of the less dominant SIF (K_{II}) can be poor and often not addressed or simply ignored. Given this, the legacy approach becomes questionable in situations involving arbitrary mode-mixity where dominance of one SIF over the other is unclear. Furthermore, for a measured field component, the accuracy of SIF obtained depends also on the region of interest from where the full-field data is extracted, as shown in [23] for mode-I experiments using CGS. Even with the widespread adoption of vision-based methods, the legacy approach of choosing a single field component for SIF extraction has continued despite multiple components being readily available.

Considering u_y as the chosen displacement for analysis in the legacy method, using the functions defined in equation (8), a set of simultaneous equations can be established [8] as:

$$\{d\} = [g]\{K\}, \quad (13)$$

where,

$$\{d\} = \begin{Bmatrix} \Sigma g_{I_1} u_y \\ \Sigma g_{I_2} u_y \\ \vdots \\ \Sigma g_{I_N} u_y \end{Bmatrix}, \{K\} = \begin{Bmatrix} K_{I1} \\ K_{I2} \\ \vdots \\ K_{IN} \\ K_{II1} \\ K_{II2} \\ \vdots \\ K_{IIN} \end{Bmatrix}, \text{ and}$$

$$[g] = \begin{bmatrix} \Sigma g_{I_1} g_{I_1} & \Sigma g_{I_2} g_{I_1} & \cdots & \Sigma g_{I_N} g_{I_1} & \Sigma g_{II_1} g_{I_1} & \Sigma g_{II_2} g_{I_1} & \cdots & \Sigma g_{II_N} g_{I_1} \\ \Sigma g_{I_1} g_{I_2} & \Sigma g_{I_2} g_{I_2} & \cdots & \Sigma g_{I_N} g_{I_2} & \Sigma g_{II_1} g_{I_2} & \Sigma g_{II_2} g_{I_2} & \cdots & \Sigma g_{II_N} g_{I_2} \\ \vdots & \vdots & \ddots & \vdots & \vdots & \vdots & \ddots & \vdots \\ \Sigma g_{I_1} g_{I_N} & \Sigma g_{I_2} g_{I_N} & \cdots & \Sigma g_{I_N} g_{I_N} & \Sigma g_{II_1} g_{I_N} & \Sigma g_{II_2} g_{I_N} & \cdots & \Sigma g_{II_N} g_{I_N} \\ \Sigma g_{I_1} g_{II_1} & \Sigma g_{I_2} g_{II_1} & \cdots & \Sigma g_{I_N} g_{II_1} & \Sigma g_{II_1} g_{II_1} & \Sigma g_{II_2} g_{II_1} & \cdots & \Sigma g_{II_N} g_{II_1} \\ \Sigma g_{I_1} g_{II_2} & \Sigma g_{I_2} g_{II_2} & \cdots & \Sigma g_{I_N} g_{II_2} & \Sigma g_{II_1} g_{II_2} & \Sigma g_{II_2} g_{II_2} & \cdots & \Sigma g_{II_N} g_{II_2} \\ \vdots & \vdots & \ddots & \vdots & \vdots & \vdots & \ddots & \vdots \\ \Sigma g_{I_1} g_{II_N} & \Sigma g_{I_2} g_{II_N} & \cdots & \Sigma g_{I_N} g_{II_N} & \Sigma g_{II_1} g_{II_N} & \Sigma g_{II_2} g_{II_N} & \cdots & \Sigma g_{II_N} g_{II_N} \end{bmatrix}$$

Here, N is the number of terms in the expansion, $\{d\}$ contains the measured displacement data, $[g]$ is a matrix of size $2N$ x $2N$ and contains the functions from Williams' asymptotic expressions, and $\{K\}$ contains the two SIFs and other higher order coefficients that must be solved for using the over-deterministic analysis. To evaluate $\{K\}$, the inverse of $[g]$ is to be evaluated:

$$\{K\} = [g]^{-1}\{d\} \tag{14}$$

Similarly, for experiments using the DGS method, the component traditionally used in the legacy approach is ϕ_x in the local crack tip coordinates. Using equation (11), the matrix equation for analysis can be established as,

$$\{\phi\} = [p]\{K\} \tag{15}$$

where,

$$\{\phi\} = \begin{Bmatrix} \Sigma p_{I_1} \phi_x \\ \Sigma p_{I_2} \phi_x \\ \vdots \\ \Sigma p_{I_N} \phi_x \end{Bmatrix}, \{K\} = \begin{Bmatrix} K_{I1} \\ K_{I2} \\ \vdots \\ K_{IN} \\ K_{II1} \\ K_{II2} \\ \vdots \\ K_{IIN} \end{Bmatrix}, \text{ and}$$

$$[p] = \begin{bmatrix} \Sigma p_{I_1} p_{I_1} & \Sigma p_{I_2} p_{I_1} & \cdots & \Sigma p_{I_N} p_{I_1} & \Sigma p_{II_1} p_{I_1} & \Sigma p_{II_2} p_{I_1} & \cdots & \Sigma p_{II_N} p_{I_1} \\ \Sigma p_{I_1} p_{I_2} & \Sigma p_{I_2} p_{I_2} & \cdots & \Sigma p_{I_N} p_{I_2} & \Sigma p_{II_1} p_{I_2} & \Sigma p_{II_2} p_{I_2} & \cdots & \Sigma p_{II_N} p_{I_2} \\ \vdots & \vdots & \ddots & \vdots & \vdots & \vdots & \ddots & \vdots \\ \Sigma p_{I_1} p_{I_N} & \Sigma p_{I_2} p_{I_N} & \cdots & \Sigma p_{I_N} p_{I_N} & \Sigma p_{II_1} p_{I_N} & \Sigma p_{II_2} p_{I_N} & \cdots & \Sigma p_{II_N} p_{I_N} \\ \Sigma p_{I_1} p_{II_1} & \Sigma p_{I_2} p_{II_1} & \cdots & \Sigma p_{I_N} p_{II_1} & \Sigma p_{II_1} p_{II_1} & \Sigma p_{II_2} p_{II_1} & \cdots & \Sigma p_{II_N} p_{II_1} \\ \Sigma p_{I_1} p_{II_2} & \Sigma p_{I_2} p_{II_2} & \cdots & \Sigma p_{I_N} p_{II_2} & \Sigma p_{II_1} p_{II_2} & \Sigma p_{II_2} p_{II_2} & \cdots & \Sigma p_{II_N} p_{II_2} \\ \vdots & \vdots & \ddots & \vdots & \vdots & \vdots & \ddots & \vdots \\ \Sigma p_{I_1} p_{II_N} & \Sigma p_{I_2} p_{II_N} & \cdots & \Sigma p_{I_N} p_{II_N} & \Sigma p_{II_1} p_{II_N} & \Sigma p_{II_2} p_{II_N} & \cdots & \Sigma p_{II_N} p_{II_N} \end{bmatrix}$$

Here, N is the number of terms. The matrix $\{\phi\}$ contains the measured angular deflections, the matrix $[p]$ has size $2N$ x $2N$ and contains the functions defined in equation (11) and $\{K\}$ contains the SIFs and higher order coefficients of the series that are solved using the over-deterministic analysis. Solving for $\{K\}$, equation (15) becomes:

$$\{K\} = [p]^{-1}\{\phi\} \tag{16}$$

In the legacy approach, the size of the matrices is determined by the number of terms used in the expansion. Using a different number of higher order terms can affect the SIF values in the legacy approach. Additionally, the summation of the $g(r,\theta)$ and $p(r,\theta)$ functions in the $[g]$ and $[p]$ matrices represent the summation of the functions across the number of data points in the region of interest. Altering the region of data points included in the analysis affects the extracted SIF values

as well. Finally, as stated previously, these functions depend on r and θ centered at the crack tip. Therefore, identifying the location for the crack tip precisely is crucial for extracting correct SIF values.

Combined Fields Approach

The combined fields approach for extracting SIFs utilizes all available components of the measured field concurrently. For 2D DIC, this involves using both components of measured displacement in conjunction with the Williams' asymptotic expressions. It leads to a matrix relationship [12]:

$$\{u\} = [g']\{K'\} \tag{17}$$

where,

$$\{u\} = \begin{Bmatrix} u_{x_1} \\ u_{x_2} \\ \vdots \\ u_{x_m} \\ u_{y_1} \\ u_{y_2} \\ \vdots \\ u_{y_m} \end{Bmatrix}, \quad \{K'\} = \begin{Bmatrix} K_{I1} \\ K_{I2} \\ \vdots \\ K_{IN} \\ K_{II1} \\ K_{II2} \\ \vdots \\ K_{IIN} \\ P \\ Q \end{Bmatrix}, \text{ and,}$$

$$[g'] = \begin{bmatrix} f_{I_1}^1 & f_{I_2}^1 & \cdots & f_{I_N}^1 & f_{II_1}^1 & f_{II_2}^1 & \cdots & f_{II_N}^1 & 1 & 0 \\ f_{I_1}^2 & f_{I_2}^2 & \cdots & f_{I_N}^2 & f_{II_1}^2 & f_{II_2}^2 & \cdots & f_{II_N}^2 & 1 & 0 \\ \vdots & \vdots & \ddots & \vdots & \vdots & \vdots & \ddots & \vdots & \vdots & \vdots \\ f_{I_1}^m & f_{I_2}^m & \cdots & f_{I_N}^m & f_{II_1}^m & f_{II_2}^m & \cdots & f_{II_N}^m & 1 & 0 \\ g_{I_1}^1 & g_{I_2}^1 & \cdots & g_{I_N}^1 & g_{II_1}^1 & g_{II_2}^1 & \cdots & g_{II_N}^1 & 0 & 1 \\ g_{I_1}^2 & g_{I_2}^2 & \cdots & g_{I_N}^2 & g_{II_1}^2 & g_{II_2}^2 & \cdots & g_{II_N}^2 & 0 & 1 \\ \vdots & \vdots & \ddots & \vdots & \vdots & \vdots & \ddots & \vdots & \vdots & \vdots \\ g_{I_1}^m & g_{I_2}^m & \cdots & g_{I_N}^m & g_{II_1}^m & g_{II_2}^m & \cdots & g_{II_N}^m & 0 & 1 \end{bmatrix}$$

Here, N is the number of terms in the expansion and m is the number of data points in the region of interest. The matrix $\{u\}$ contains both the x- and y-field components of the measured displacement data and rigid body terms P and Q, and the matrix $\{K'\}$ contains the SIFs and the higher order coefficients that are solved for by performing the over-deterministic linear least-squares error minimization. The matrix $[g']$ contains functions $f(r,\theta)$ and $g(r,\theta)$, and a series of 1 and 0 coefficients for the P and Q rigid body terms. Again, the subscripts I and II denote mode-I or mode-II functions, respectively, and the subscript N denotes the higher order term the function relates to. In the legacy method, the functions in the matrix are summed across all terms in the region of interest. In the combined fields method, this summation occurs as a result of evaluating equation (17) rather than occurring in the matrix directly. Because of this, an additional superscript is added to denote the data point that each function is related to for all points in the region of interest. The superscripts numbered 1 through m in the $[g']$ matrix correspond to the subscripts in the $\{u\}$ matrix. The coefficients in $\{K'\}$ can be solved as,

$$\left([g']^T[g']\right)^{-1}[g']^T\{u'\} = \{K'\} \tag{18}$$

Note that because $[g']$ generally has a different number of rows ($2\,m$) than columns ($2N+2$), a standard matrix inversion is not possible. By multiplying $[g']$ and its transpose $[g']^T$ a new matrix that can be inverted is made for solving $\{K'\}$ and extract values of all the coefficients.

For experiments using DGS, both orthogonal components of the measured angular deflection fields are used concurrently. The same logic as in DIC is used here to solve a set of linear equations:

$$\{\phi'\} = [p']\{K'\} \tag{19}$$

where,

$$\{\phi\prime\} = \begin{Bmatrix} \phi_{x_1} \\ \phi_{x_2} \\ \vdots \\ \phi_{x_m} \\ \phi_{y_1} \\ \phi_{y_2} \\ \vdots \\ \phi_{y_m} \end{Bmatrix}, \quad \{K'\} = \begin{Bmatrix} K_{I1} \\ K_{I2} \\ \vdots \\ K_{IN} \\ K_{II1} \\ K_{II2} \\ \vdots \\ K_{IIN} \end{Bmatrix}, \text{ and}$$

$$[p'] = \begin{bmatrix} p_{I_1}^1 & p_{I_2}^1 & \cdots & p_{I_N}^1 & p_{II_1}^1 & p_{II_2}^1 & \cdots & p_{II_N}^1 \\ p_{I_1}^2 & p_{I_2}^2 & \cdots & p_{I_N}^2 & p_{II_1}^2 & p_{II_2}^2 & \cdots & p_{II_N}^2 \\ \vdots & \vdots & \ddots & \vdots & \vdots & \vdots & \ddots & \vdots \\ p_{I_1}^m & p_{I_2}^m & \cdots & p_{I_N}^m & p_{II_1}^m & p_{II_2}^m & \cdots & p_{II_N}^m \\ q_{I_1}^1 & q_{I_2}^1 & \cdots & q_{I_N}^1 & q_{II_1}^1 & q_{II_2}^1 & \cdots & q_{II_N}^1 \\ q_{I_1}^2 & q_{I_2}^2 & \cdots & q_N^2 & q_{II_1}^2 & q_{II_2}^2 & \cdots & q_{II_N}^2 \\ \vdots & \vdots & \ddots & \vdots & \vdots & \vdots & \ddots & \vdots \\ q_{I_1}^m & q_{I_2}^m & \cdots & q_{I_N}^m & q_{II_1}^m & q_{II_2}^m & \cdots & q_{II_N}^m \end{bmatrix}$$

In these matrices, N is the number of terms in the expansion and m is the number of data points in the region of interest. The matrix $\{\phi'\}$ contains both the x- and y-components of the measured angular deflections of light rays, and the matrix $\{K'\}$ contains the SIFs and coefficients that are solved for by performing the over-deterministic least-squares analysis. The matrix $[p']$ contains the functions $p(r,\theta)$ and $q(r,\theta)$. The subscripts I and II denote the function related to the mode-I or mode-II, respectively, and the subscript numbering up to N denotes which higher order term the function relates to. As in DIC, functions in the matrix were summed across all terms in the region of interest in the legacy method, but in the combined fields method, this summation occurs as a result of evaluating equation (19) rather than

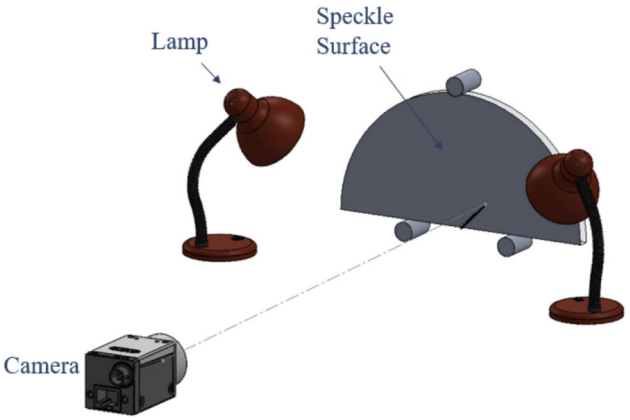

Fig. 3 Schematic of the experimental setup for DIC

occurring in the matrix directly. Therefore, an additional superscript is added again to denote the data point that each function is related to. The superscripts numbered 1 through m in the $[p']$ matrix correspond with the numbering of the subscripts in the $\{\phi'\}$ matrix. Now, $\{K'\}$ can be solved as,

$$\left([p']^T[p']\right)^{-1}[p']^T\{\phi'\} = \{K'\} \tag{20}$$

For both the DIC and DGS methods, the size of the matrices is determined by both the number of terms N and the number of data points m in the region of interest. This is unlike the legacy method where the matrix sizes are determined only by the number of terms N. Therefore, N value chosen in the analysis and the number of data points m included in the region of interest will both influence the extracted SIFs. Additionally, the functions $f(r,\theta)$, $g(r,\theta)$, $p(r,\theta)$, and $q(r,\theta)$ depend on the polar coordinates r and θ, which are in the coordinate system with the origin centered at the crack tip. Therefore, imprecise location of the crack tip can affect the values of SIFs.

Experimental Setup: DIC

For performing experiments using DIC, a random speckle pattern was applied to one of the two faces of the SCB specimen by spraying black and white paints successively. The specimen was subsequently subjected to three-point bending. Two white light sources were used for illuminating the specimen uniformly and the recording was done using a Point-Grey 4 Mpx camera. The schematic of the experimental setup is shown in Fig. 3.

An Instron-4455 mechanical testing machine was used to load the specimen from 0 to 1500 N in the displacement control mode with a crosshead speed of 0.5 mm/s. During ramp loading, both the load and loading-pin displacement data were recorded. Simultaneously, the speckle images from the specimen surface were captured at specific load steps at a rate of 2 fps. Images that correspond to load steps of 100 N were then selected and post-processed using ARAMIS

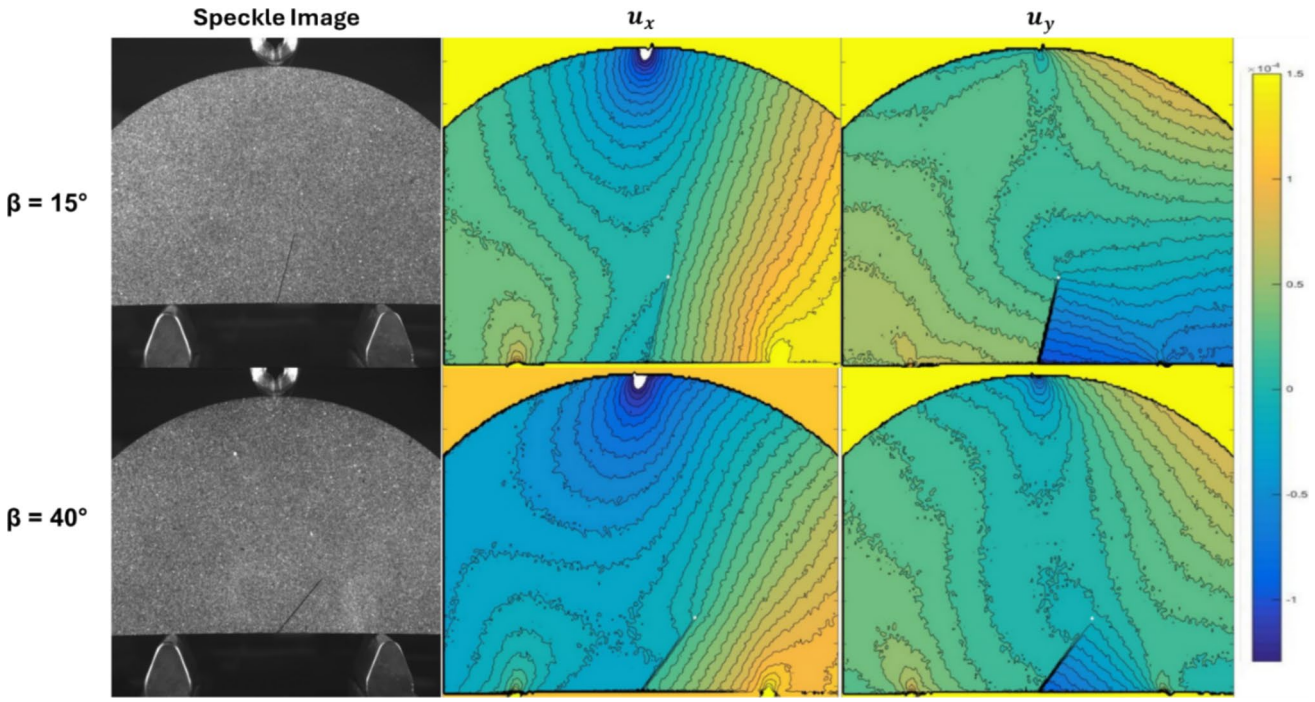

Fig. 4 The recorded speckle images (column 1), displacement components u_x and u_y contours (in local coordinates) from DIC (columns 2 and 3) (contour increments: 10 μm)

image analysis software with the no-load image as the reference image. Examples of the resulting displacement contours are shown in Fig. 4 for two different crack angles at the maximum load level of 1500 N. The camera parameters and image analysis software specifics are listed in Table 2.

The contour plots in Fig. 4 show the measured displacement fields in the *local* crack tip coordinates. All four plots have a contour spacing of 10 μm/contour. Both sets show mixed-mode crack tip deformations and the influence of the loading pin and the two supports. For $\beta = 15°$ geometry, the u_y contours show a larger crack opening displacement relative to $\beta = 40°$ case as it is relatively mode-I dominant. In $\beta = 40°$ case, on the other hand, the contours show a larger crack sliding displacement u_x as mode-II conditions are more pronounced.

Results and Discussion: DIC

The values of SIFs K_I and K_{II} extracted from the DIC experiments using both the legacy and the combined fields approaches are compared with each other in Fig. 5, with each row for a different crack angle and the second and third columns showing the two SIF extraction approaches. As noted earlier, the five crack angles chosen cover the entire range of mode-mixities, from pure mode-I to mode-II.

In Fig. 5, the solid and open symbols (squares and circles) correspond to mode-I and mode-II SIF values, respectively. The predicted results are shown as solid and dotted lines. Each plot covers the SIF values over the loading range of 0–1500 N. The measured data in the range $0.5 < r/B < 1.5$ (B = thickness) and $-135° < \theta < 135°$ was used for both the legacy and the combined fields approaches. This was to exclude any crack tip triaxial deformation and free surface effects in the region too close to the crack flanks, as well as for excluding the effects of the loading and support pins. In addition, both the legacy and the combined fields methods used $N = 4$ terms. The improvements seen by utilizing both orthogonal displacement field components in tandem is evident in all of the plots, with an overall increase in the accuracy and precision relative to the theoretical solution. For the legacy approach, there is noticeable scatter in the K_I values and substantial scatter for K_{II} values across all crack angles. That said, the legacy K_I values are close to the expected theoretical ones. On the other hand, when using the combined fields approach, both SIF values show a consistent, more precise and linear progression. More importantly, the values of both SIFs closely match the respective predictions with greater accuracy and precision. The deviations that exist in the data are due to inherent noise in the measured data, likely error in selecting a crack tip location, selected region of interest, or a combination of these factors. For all angles, the effect from these sources of error is visibly more significant when using the legacy approach than the combined fields approach.

In order to further characterize the improvement of the combined fields method, additional analysis parameters were varied to demonstrate its robustness relative to the legacy approach. For brevity, the results corresponding to only the maximum load (1500 N) are shown here. The selected parameters during analysis were the number of higher order terms used, the location of the crack tip that was selected, as shown in Fig. 6(a) and the region of interest utilized in the analysis (Fig. 6(b)). When an extraction method is robust, the effects of altering these parameters will be minimum. The variation in the extracted SIF values from these parametric variations were compared qualitatively and quantitatively to determine the better of the two approaches.

For a method to be considered robust, it should be capable of extracting consistent and accurate values of SIFs across multiple different parameterized iterations, indicating that the results that are produced are not merely due to an operator input but are displaying the experimental outcome accurately. To assess this, the highest load-step is iterated across different numbers of higher order terms N in the asymptotic series. By truncating the series after a certain number of terms, we can also identify if there is an ideal number of higher order terms to use in the analysis for the geometry, or if the method is robust enough to successfully extract SIFs for a range of N values. These results are shown in Fig. 7.

By comparing the plots in Fig. 7, the two extraction techniques can be contrasted for the same specimen geometry at a fixed load. Note that for each row of plots, the second and third columns describe the results from the same experimental data but a different extraction approach. The gray solid and dashed lines represent the predicted values. The solid symbols (squares and circles) represent the extracted values for K_I and the open symbols represent K_{II}. It is noteworthy that the experiments may not have perfectly replicated the predictions due to experimental and post-processing errors, and therefore deviations of less than 5% from the predictions are considered acceptable. By comparing the combined fields method to the legacy approach, the improvements become rather clear. Although both methods produce similar data trends, the combined fields approach does a significantly better job of extracting the trend consistently across any number of terms N of the experiment with deviations of less than 2%. While K_I for the legacy approach is acceptable, the K_{II} values vary significantly with load (standard deviation $\approx 1\text{MPa}\sqrt{\text{m}}$) and seem to not adhere to an explainable trend. In contrast, the tight grouping of values of both K_I and K_{II} in the combined fields method shows the robustness and gains in both accuracy and precision. As can be seen, the legacy method performs poorly while extracting consistent values of SIFs in comparison to the combined fields

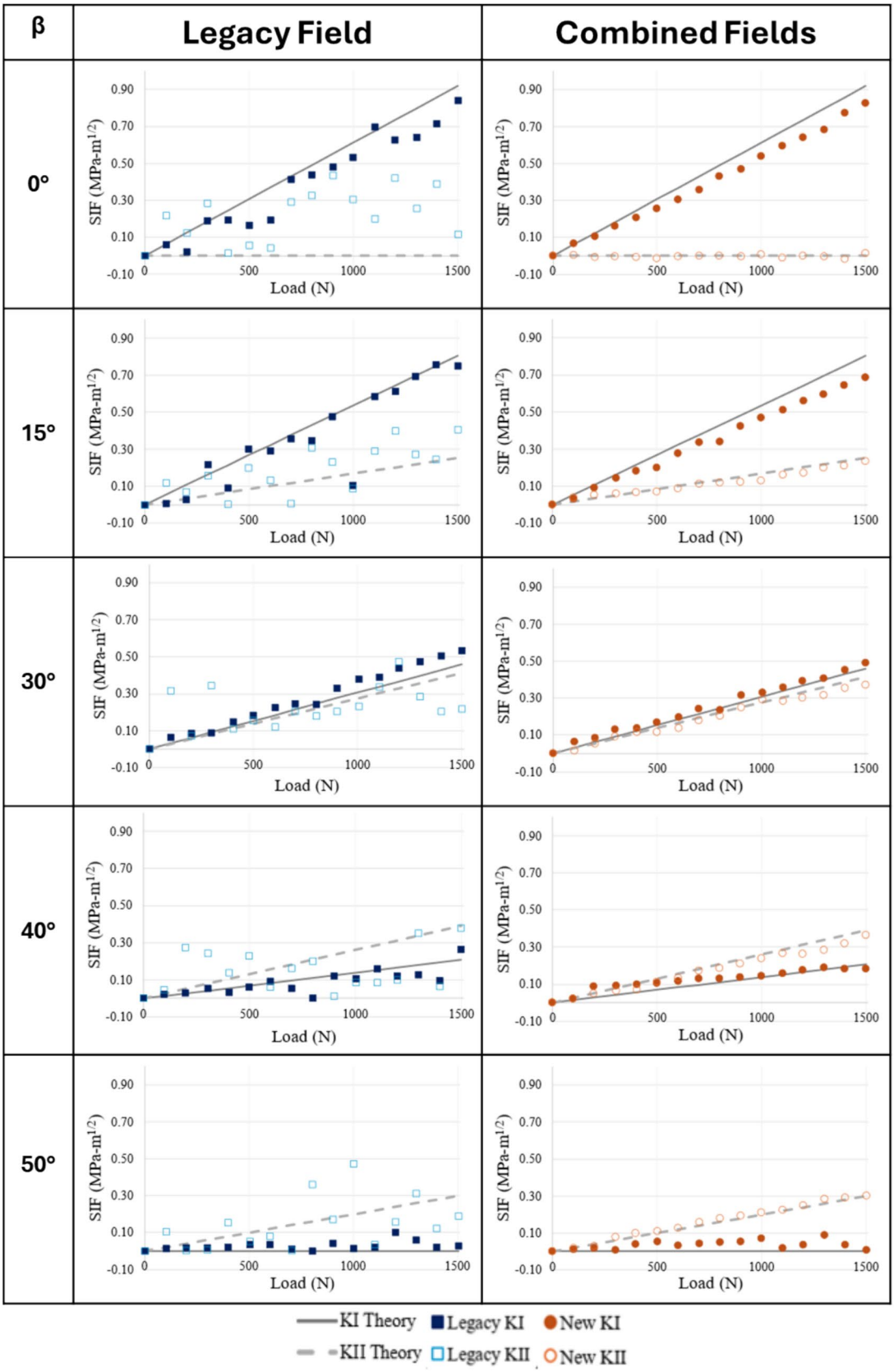

Fig. 5 SIFs at different loads for different crack angles and different extraction approaches using measured displacements from DIC. (Legacy method uses u_y field in the analysis)

Table 2 Camera specifications and image analysis features

Hardware Parameters		Analysis Parameters	
Camera Manufacturer	Point Grey	Software Package	ARAMIS v6.3.1
Camera Model	Grasshopper3 GS3-U3-41C6M	Software Manufacturer	GOM
Image Resolution	2048 × 2048 px	Image Filtering	None
Lens Manufacturer	Computar Lens	Sub-image Size	20 px
Focal Length	18—108 mm	Step Size	10 px
Field of View	98 × 98 mm	Subset Shape Function	Affine
Image Scale	0.048 mm/px		
Stand-off Distance	1 m		
Image Acquisition Rate	2 fps		
Patterning Technique	Spray Painted		
Approx. Feature Size	5 px		

method. For $\beta = 0^o$ case, even though the K_I values are close to the predicted value, K_{II} values are far from the prediction. For every subsequent geometry, the deviation between the extracted values of the same experiment as N is increased indicates scenarios where two operators working with the same data set could extract values as much as 50% different from the legacy method. In contrast, with the values being very similar for $N \geq 3$ as well as K_I and K_{II} are both accurate, once again the precision of the combined fields method is clear. This difference indicates once again that using all orthogonal fields simultaneously is more robust to changes in the number of higher order terms than the legacy method, resulting in SIFs having greater consistency.

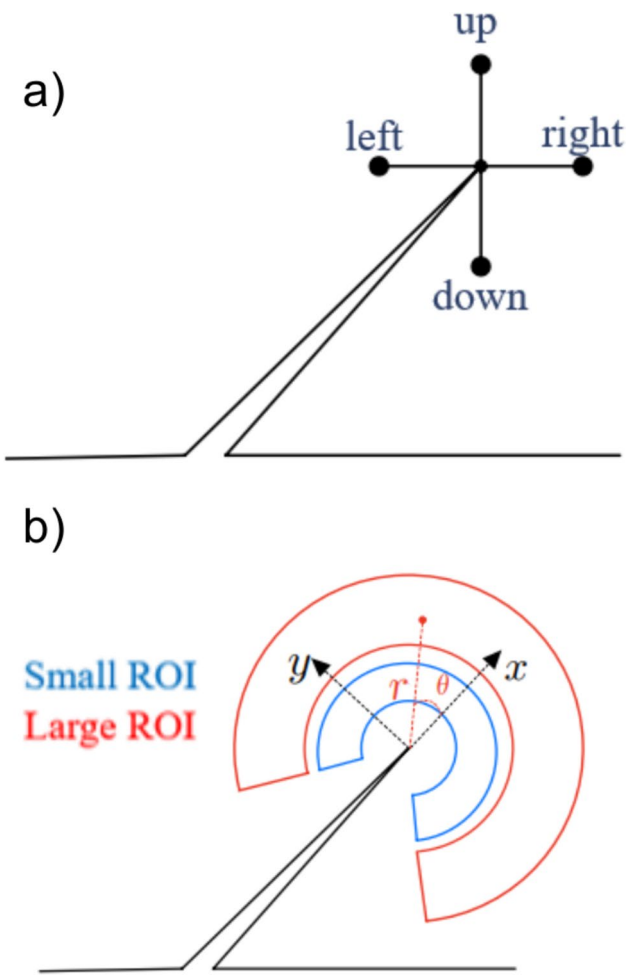

Fig. 6 Schematic representation of varying **a** crack tip position, **b** region of interest during analysis

Next, the robustness of the method to crack tip selection errors was assessed at a fixed load of 1500 N. In Fig. 8, five sets of SIF results are shown on each plot. These five sets were acquired by altering the position of the crack tip as shown in Fig. 6(a). This variation in crack tip selection is meant to simulate an experimental error that could occur due to operator error during analysis. The crack tip location was intentionally altered by a distance of 10 pixels in each of the four directions: up, down, left, and right, as shown, relative to the initial pick. Including the original crack tip selection, the outcomes consist of five distinct SIF data series. Each of these are displayed in Fig. 8 for the number of terms N up to 15. Closed symbols are used to denote K_I and open ones denote K_{II}. Again, the solid and dashed lines represent the predicted values. The columns two and three show results for the legacy and the combined fields approach. Since the same observation occurs in all geometries, only $\beta = 15°$ and $\beta = 40°$ are shown here as representative examples. For the $\beta = 15°$ geometry, the legacy approach of extracting K_I drifts away from the prediction for a higher number of terms N and has a significant amount of variation (standard deviation $= 0.258\text{MPa}\sqrt{\text{m}}$). In addition, the legacy method has a large spread when extracting K_{II} (standard deviation $= 1.099\text{MPa}\sqrt{\text{m}}$). On the other hand, the combined fields approach extracts a consistent value for K_I and K_{II} for all five crack tip selections. The variation for the new approach (standard deviation $< 0.025\text{MPa}\sqrt{\text{m}}$) is an order of magnitude lower than the legacy approach. For the $\beta = 40°$ the new method again extracts much more consistent

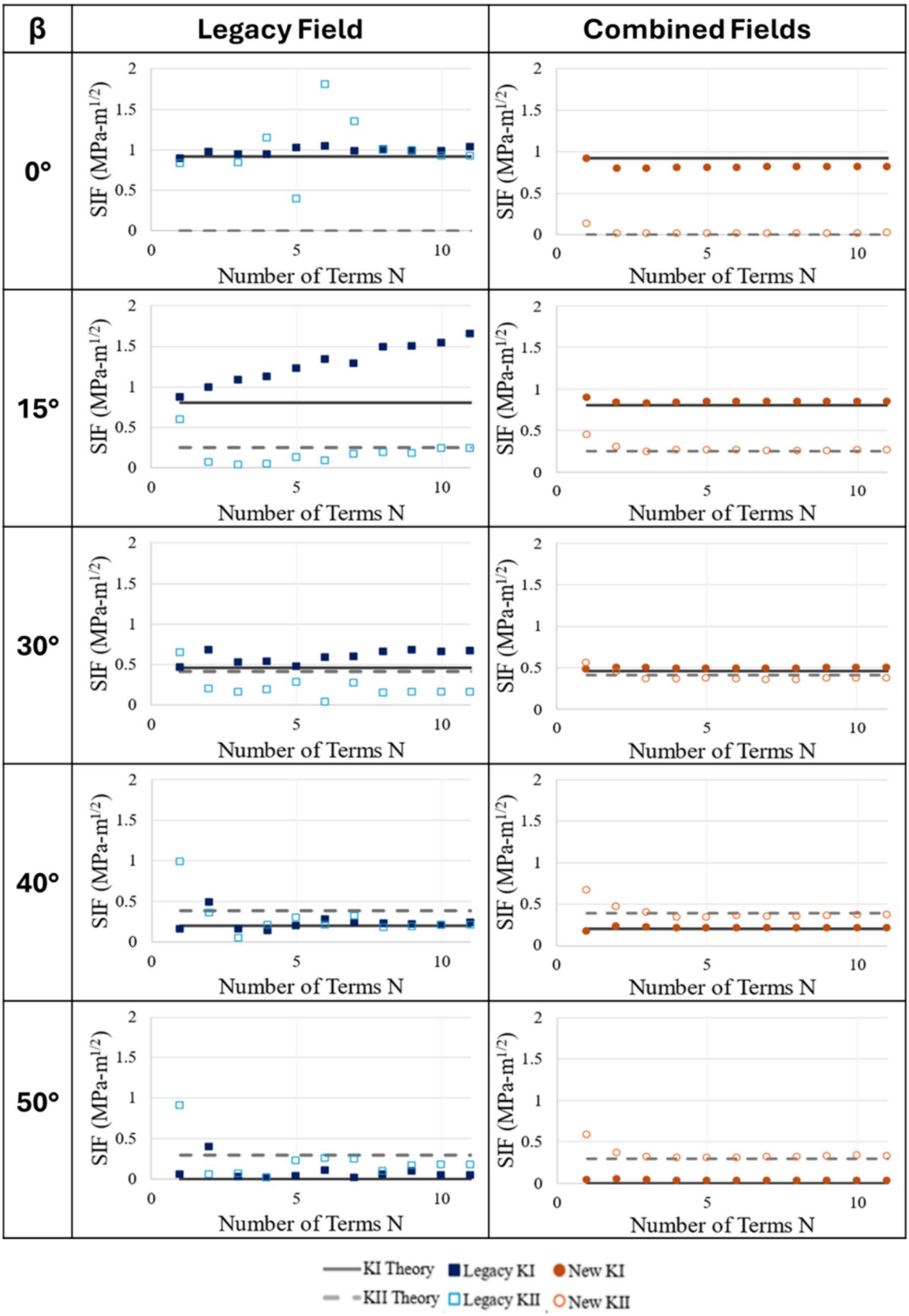

Fig. 7 Variation of SIFs for different higher order terms in the asymptotic expansion for the legacy and combined fields approaches using DIC. (Legacy method used u_y field in the analysis)

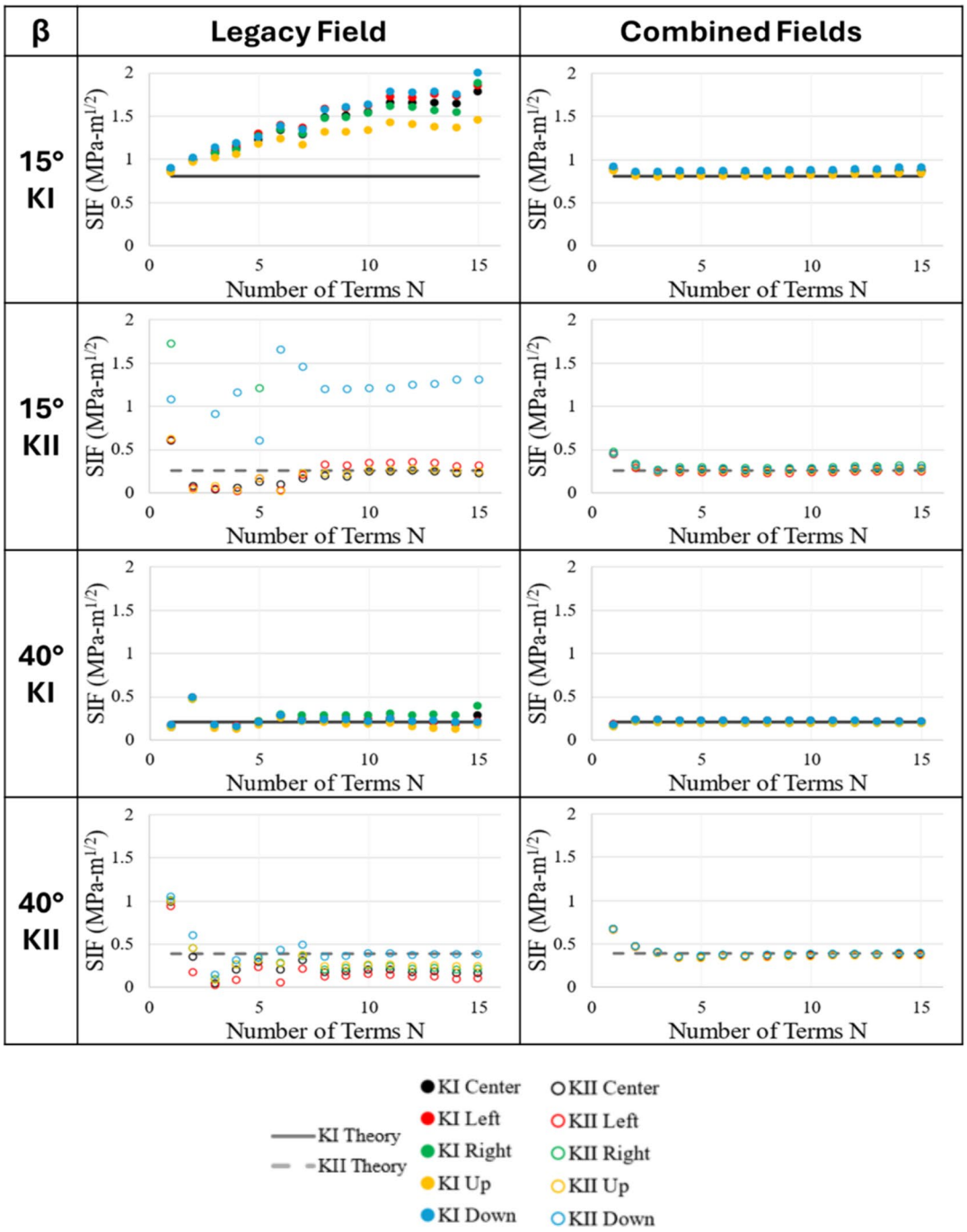

Fig. 8 Variation of SIFs due to different crack tip position selection in the legacy and combined fields approaches using DIC. (Legacy method uses u_y field in the analysis)

values for SIFs. The standard deviation in the data extracted using the new approach is more than 50% lower than the legacy counterpart. Additionally, the extracted values of SIFs using the new method match the predicted values much more closely. Overall, this results in a significantly lower cumulative crack tip error for the combined fields method in comparison to the legacy approach.

In Fig. 9 two sets of results are shown on each plot representing data extraction in the large and small regions of interest (Fig. 6(b)). The original region of interest was $0.5 < r/B < 1.5$ and $-135° < \theta < 135°$. Additional regions of interest were created with the limits on θ unchanged, but the r/B range was decreased and increased relative to the original. For the smaller region of interest, the range was

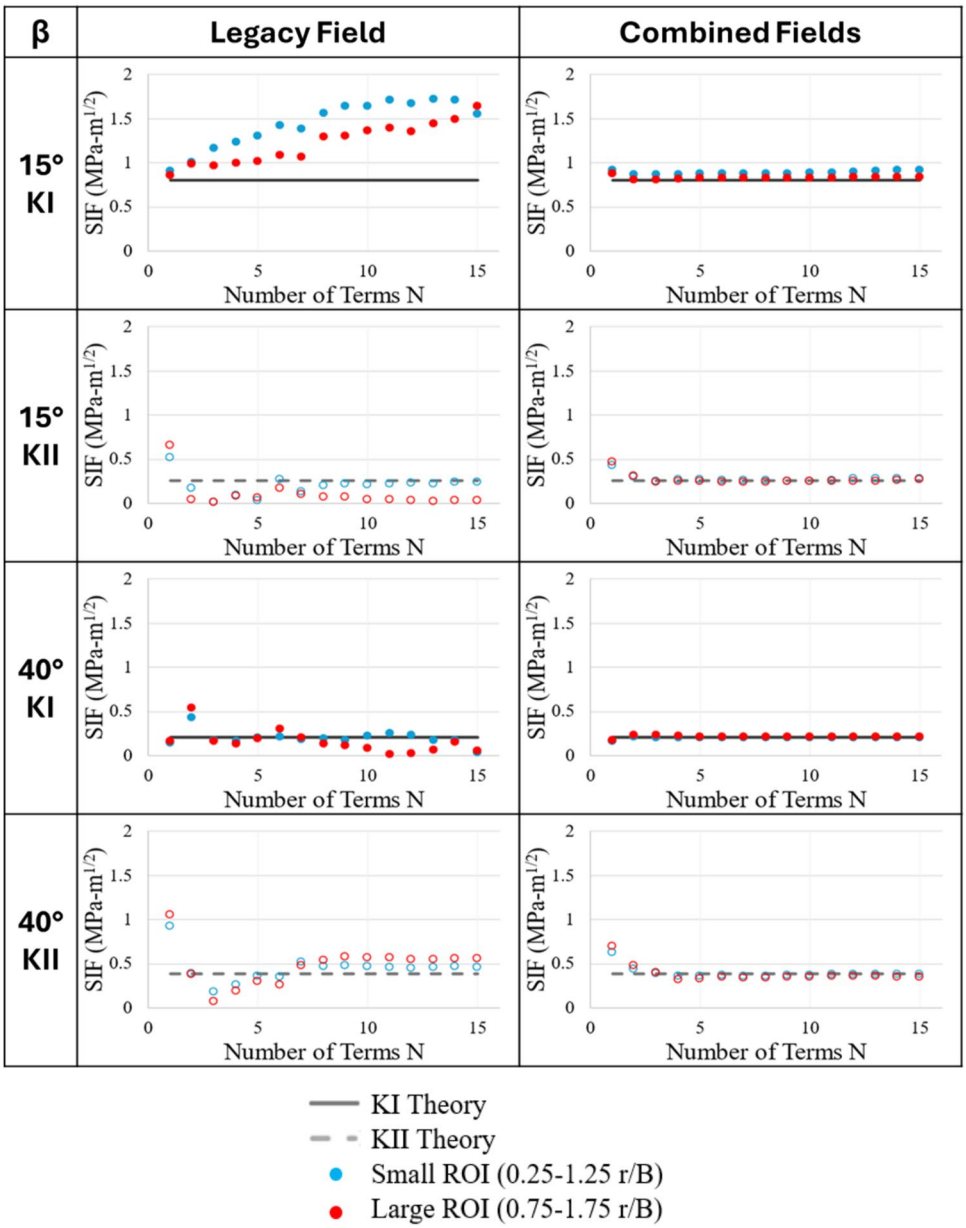

Fig. 9 Variation of SIFs for two different regions of interest for the legacy and combined fields approaches using DIC. (Legacy method uses u_y field in the analysis)

$0.25 < r/B < 1.25$ and for the larger region of interest, the range was $0.75 < r/B < 1.75$. The results extracted using both regions of interest are displayed in Fig. 10 at 1500 N and for a number of terms up to $N = 15$. Note that the results for the original region of interest are not repeated here for brevity and clarity of plots.

As before, the closed symbols are used when plotting K_I and open symbols for K_{II}. The solid and dashed lines represent the predicted values. The same trend is seen in all five geometries but for brevity the ones for $\beta = 15°$ and $\beta = 40°$ are shown as representative examples. In the $\beta = 15°$ case, the legacy approach extracts K_I with a standard deviation of $0.250\text{MPa}\sqrt{\text{m}}$ and K_{II} with standard deviation of $0.087\text{MPa}\sqrt{\text{m}}$. This is significantly improved in the combined field approach which extracts K_I with standard deviation of $0.058\text{MPa}\sqrt{\text{m}}$ and K_{II} with a standard deviation of $0.017\text{MPa}\sqrt{\text{m}}$. For the $\beta = 40°$ geometry, similar improvements are seen as well.

To summarize the improvements in robustness seen by using the combined field method, Tables 3 and 4 include the standard deviation and root mean square error (RMSE) for the SIF results shown in Figs. 8 and 9, respectively. The standard deviation represents the average deviation in the extracted SIF without regard to the predicted value, while the RMSE represents the

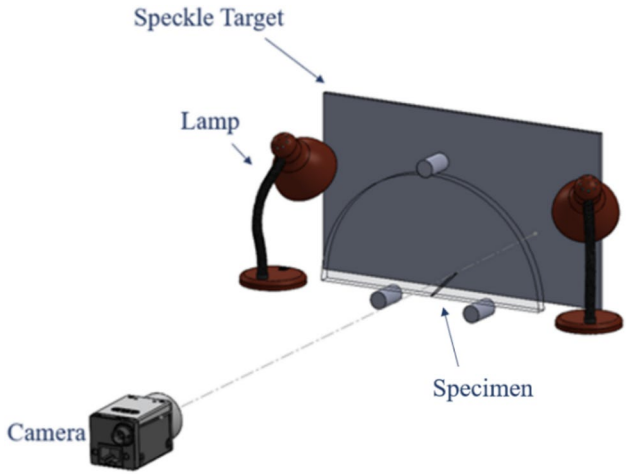

Fig. 10 Schematic of the experimental setup used for DGS

average error SIFs have from the predicted value. In a perfectly robust technique, the standard deviation and RMSE would both be zero, as there would be no deviation regardless of the changes to the parameters. For both of these quantities, the new approach consistently has lower deviation and lower error for all crack angle geometries and mode-mixites.

Experimental Setup: DGS

For transmission mode DGS, instead of creating a speckle pattern on the specimen surface, the PMMA specimen was left transparent, and a planar, randomly speckled target was placed parallel to and behind the specimen plane at a known distance $\delta(= 30\text{mm})$, see Fig. 10. A pair of white light sources illuminated the speckled target uniformly. Note that the target surface was prepared by spraying black and white paints successively as done in DIC counterpart. During the experiment, the camera recorded the speckles on the target plane through the transparent specimen. Thus, the perceived displacements of speckles on the target plane due to changes in local refractive index of the transparent material and its thickness due to the Poisson effect were encoded in each image. In the post-processing step, the speckle images in the deformed state were correlated with the one in the reference state to evaluate pseudo-displacement of speckles. Knowing δ (Fig. 2), the angular deflections of the light rays that are proportional to the local stress gradients as in Eq. 3 were obtained and mapped to the specimen plane using paraxial approximation. Aside from the transparent nature of the specimen and the focusing of the camera on the speckle target behind the specimen plane, the experiments were identical to DIC counterparts. Other imaging and speckle correlation parameters used for DGS were a scale factor of 0.057 mm/px, sub-image size of 30×30 px and a step size of 3 px and were implemented again using ARAMIS image analysis platform.

Table 3 SIF variation due to crack tip selection in DIC

Geometry	Approach	Standard Deviation (MPa$\sqrt{\text{m}}$)	RMSE (MPa$\sqrt{\text{m}}$)
$\beta = 15^{\circ}$	Legacy K_I	0.2579	0.8499
	Legacy K_{II}	1.0992	1.2777
	Combined K_I	0.0235	0.0475
	Combined K_{II}	0.0240	0.0251
$\beta = 40^{\circ}$	Legacy K_I	0.0847	0.1238
	Legacy K_{II}	0.1147	0.1828
	Combined K_I	0.0117	0.0119
	Combined K_{II}	0.0303	0.0393

Table 4 SIF variation due to region of interest selection in DIC

Geometry	Approach	Standard Deviation (MPa$\sqrt{\text{m}}$)	RMSE (MPa$\sqrt{\text{m}}$)
$\beta = 15^{\circ}$	Legacy K_I	0.2500	0.6243
	Legacy K_{II}	0.0866	0.1490
	Combined K_I	0.0279	0.0525
	Combined K_{II}	0.0172	0.0182
$\beta = 40^{\circ}$	Legacy K_I	0.1055	0.1054
	Legacy K_{II}	0.1570	0.1602
	Combined K_I	0.0083	0.0085
	Combined K_{II}	0.0315	0.0394

Results and Discussion: DGS

As discussed in the case of DIC results, both the legacy and the combined fields approach of extracting pure and mixed-mode SIFs were implemented for all five crack angles of the SCB geometry. For brevity, the angular deflections in local crack tip coordinates are plotted for two mixed-mode cases as color coded contours in Fig. 11. Here the contours are plotted from -250 µrad to 250 µrad in steps of 18 µrad.

In the case of $\beta = 15^{\circ}$ geometry, the contours around the crack are more pronounced when compared to the $\beta = 40^{\circ}$ contours due to the dominance of mode-I behavior in the geometry, resulting in a relatively higher deflection of light rays. Both ϕ_x and ϕ_y contours present a tri-lobed structure, which is more readily evident in the former whereas one of the three lobes in the latter is indistinguishable due to the close alignment of those lobes with the noisy crack flanks. *It is important to note that, in contrast to DIC contours, the values of angular deflections in DGS are the highest near the crack tip and decrease rapidly with r.* This leads to a severe concentration of data around the tip of the crack (as well as at the two vertical

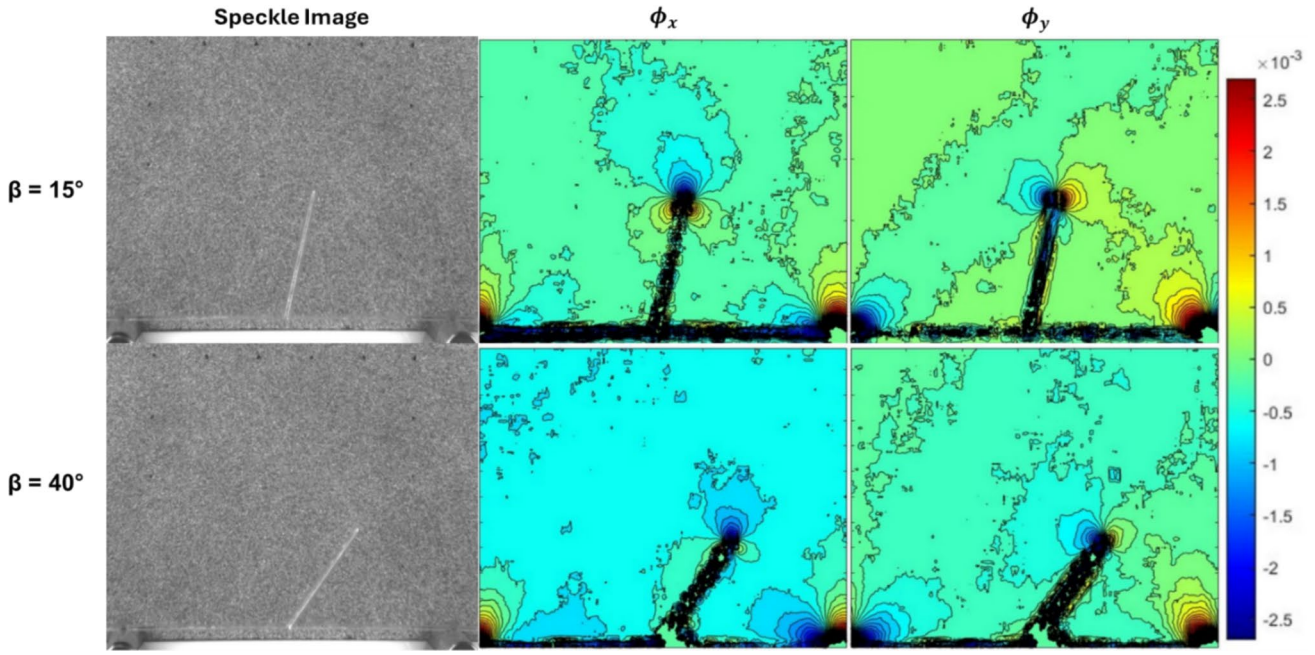

Fig. 11 The recorded speckle images (column 1), contours of angular deflections ϕ_x and ϕ_y (in local coordinates) DGS (columns 2 and 3) (contour increments: 18 μradians)

supports), and the large regions of small values in regions far away from the crack tip. Thus, the stress gradients in regions far from the crack tip have higher relative error and noise. The SIF results obtained and observations made by analyzing these measurements show similarities and differences from those for the DIC counterparts and are discussed below.

In Fig. 12, the variation of mode-I and -II SIFs at different load levels (0-1500 N) from both the legacy and the combined fields approaches are shown in two columns for all five crack angles. Again, similar to the DIC results, the solid and open symbols in Fig. 12 represent K_I and K_{II}, respectively, with squares and circles used for the legacy and new approaches. The measured DGS data in the region $0.4 < r/B < 1.3$ and $-135° < \theta < 135°$ were used for both the legacy and combined fields approaches. For the legacy method, the analysis used the ϕ_x component of equation (3) (x and y defined in the local crack tip coordinates, see Fig. 1). On the contrary, both ϕ_x and ϕ_y were used concurrently in the combined fields approach. The results from both the approaches are compared to the predicted values of K_I and K_{II}, shown as solid and broken lines. Note that $N = 4$ terms was used for both approaches. In each of these plots, a linear variation of SIFs with load is evident. In all the five crack angles, a good agreement between the legacy and combined fields with the respective predictions is seen over the entire load range. (Note that due to unavoidable experimental errors, marginal deviations from the predicted solutions in either extraction approach is expected and considered acceptable.) This is unlike the DIC results where the combined fields method was found clearly superior to the legacy approach. That is, where in the DIC experiments the legacy approach performed far worse than the combined fields approach in terms of accuracy and robustness, in the DGS experiments the two performed somewhat comparably. In many cases, the legacy method was as good as the combined fields method. This is likely due to the nature of what DGS measures, namely the spatial derivatives of stresses (see equation (3)). Note that the stress gradient fields do not contain the constant term (the so-called T-stress term) in the William's asymptotic equation. Additionally, in DGS the crack tip vicinity experiences larger magnitude angular deflections of light rays relative to distant locations where stress gradient data for the analysis come from. This is unlike DIC where displacement magnitudes are small near the crack tip and increase with r. Due to this, DGS results do not stand to gain a substantial improvement as in the DIC counterparts in terms of accuracy from the combined fields method.

To quantify the gains the combined fields approach offers in terms of robustness, the analysis was subjected to a series of parameterized variations at a single load-step to determine what errors the said variations induce. A robust method would have a lower disagreement between the extracted outputs when the parameters were varied within the analysis. The first of these variations utilized the maximum load-step of 1500 N, and the number of higher order terms N in the asymptotic series in equations (9) and (10) was varied from 1 to 10 terms. The results of this analysis are shown in Fig. 13. The rows represent each of the

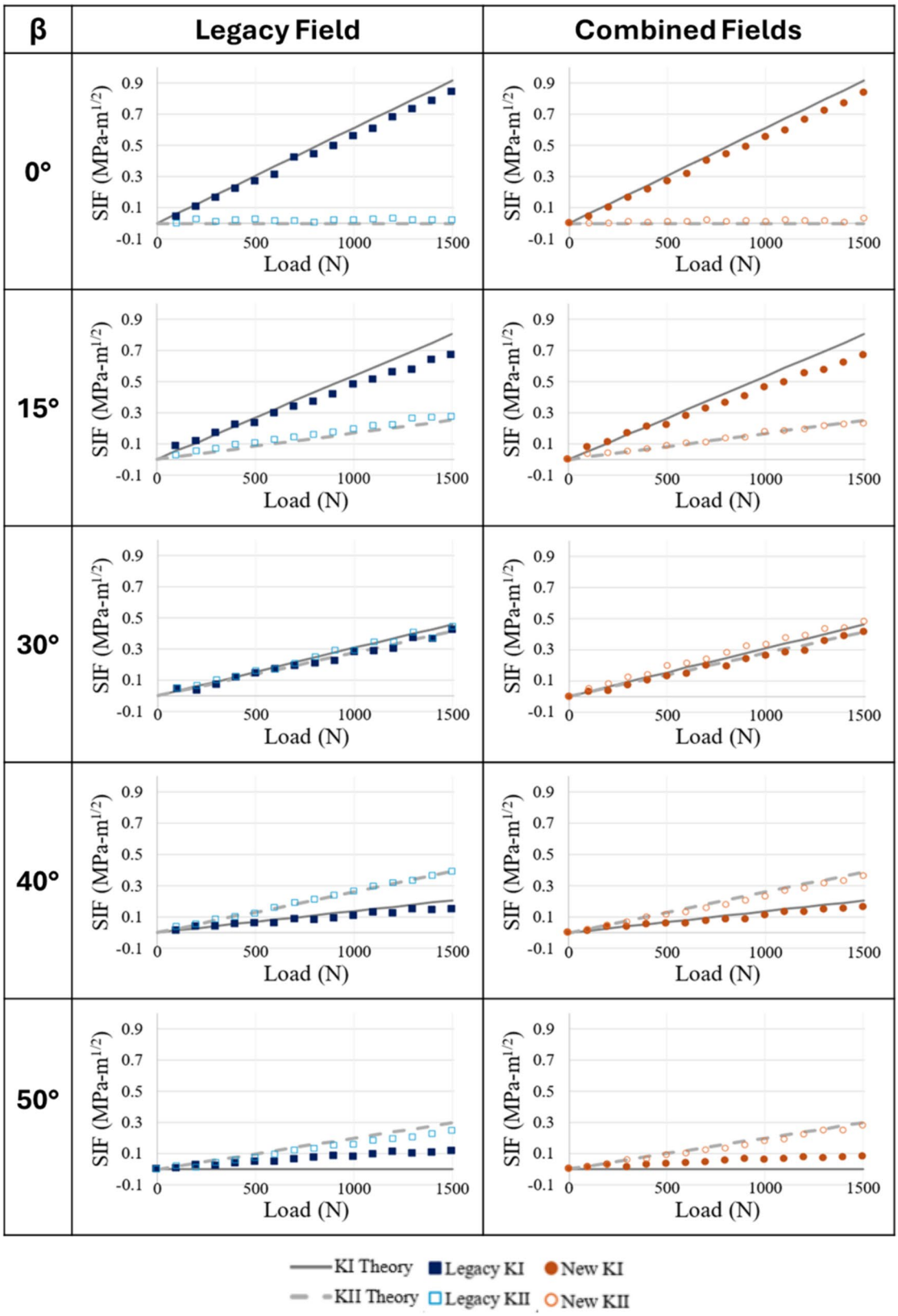

Fig. 12 SIFs at different loads for different crack angles and different extraction approaches using measured displacements from DGS. (Legacy method uses ϕ_x field in the analysis)

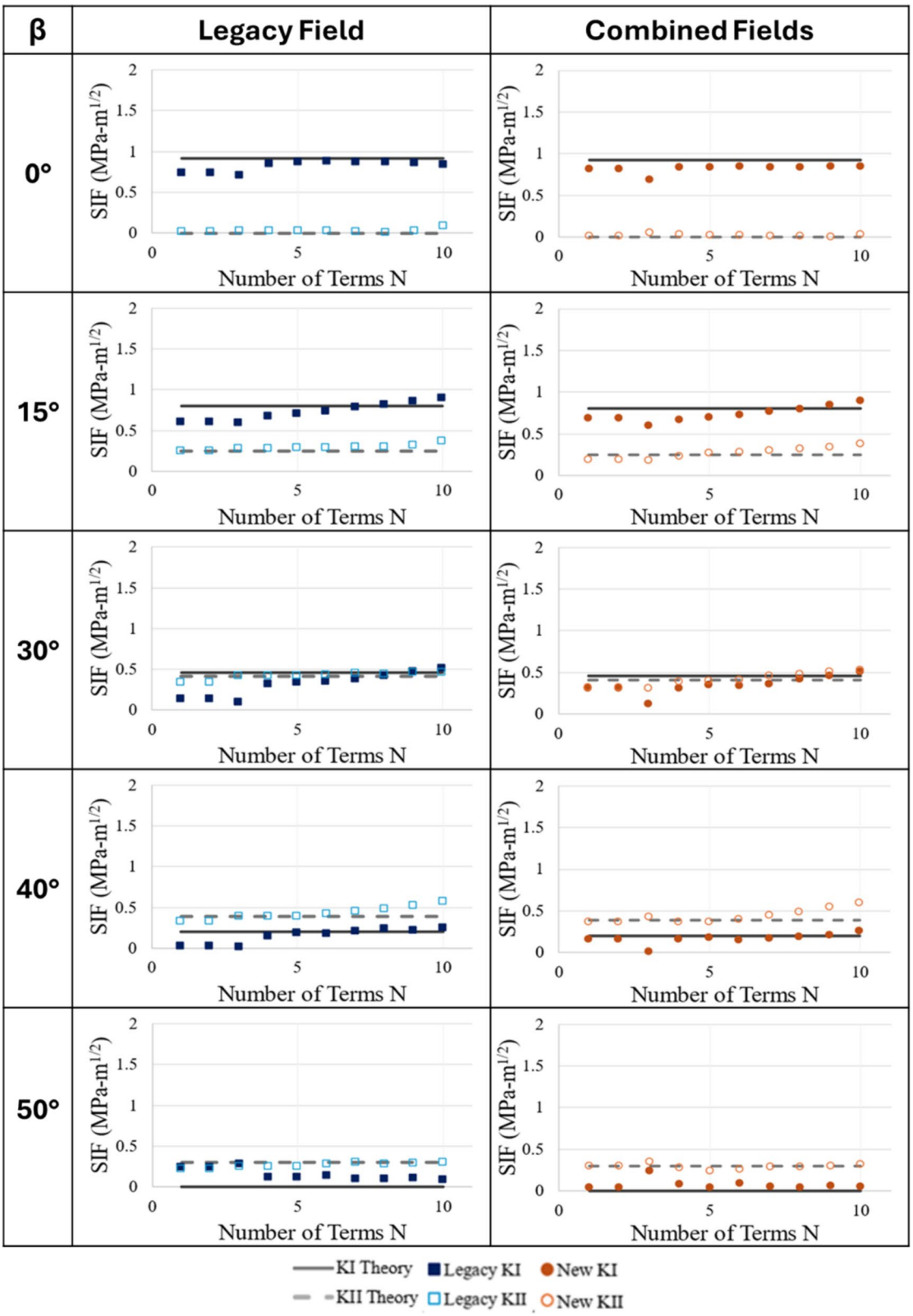

Fig. 13 Variation of SIFs for different number of higher order terms in the asymptotic expansion for the legacy and combined fields approaches using DGS. (Legacy method uses ϕ_x field in the analysis)

five crack angles, and the columns represent the analysis approach used. As in DIC results, in each of the graphs, the extracted value of K_I and K_{II} is designated by a solid or open symbol, respectively, with the legacy approach defined by squares and the combined field approach by circles. The theoretical solutions are designated by the solid and dashed lines for K_I and K_{II}, respectively. The desired solution is for each series of extracted SIF values to represent the theoretical solution across any value of N.

Comparing the results across columns in Fig. 13, one can observe that SIFs show greater deviation from the theory when fewer higher order terms were used in the legacy approach. This however is generally not the case when both gradient fields were used concurrently in the combined fields approach. That said, both approaches do provide similar SIF results when $N > 3$. That is, both approaches offer accurate values for both K_I and K_{II}, indicating that different operators using different numbers of higher order terms would extract similar values. For example, in the $\beta = 30°$geometry, the legacy approach keeps the extracted values of K_I and K_{II} to approximately 10% deviation if $N > 3$. Although the combined field approach performs slightly better than the legacy method, both approaches produce deviations small enough to be considered acceptable. This same observation can be made for all five crack angles, with the mixed-mode cases exhibiting the same behavior as the pure mode-I and mode-II cases. It is worth noting that previous investigations have typically used $N = 4$ to extract SIFs from DGS fields [6], and the current results seem to support that choice. It is also generally uncommon to employ N to be less than 3 as the higher order terms typically do influence SIF in finite specimen geometries when specimen edges are close to the crack tip.

The next factor of robustness to examine was to compare the ability of each approach to produce reliable results despite inaccuracies in crack tip selection. The determination of the crack tip location is subject to human error more so in DGS than DIC; there is often a small region where the crack tip of the specimen is likely located, as opposed to an individual point of high certainty. Due to this, experimentalists using the DGS method stand to gain from an approach which is robust against error in the presumed crack tip location. To quantify this, the maximum load-step of 1500 N was considered as before, and a crack tip location was picked as the origin. The crack tip was then varied a distance of ten pixels to the four neighboring points (see Fig. 6(a)) in the analysis, and the results are plotted as a series of five points at each N. An ideal solution would be for all five points to overlap, describing the same value regardless of which crack tip location was considered during the analysis. The results are plotted in Fig. 14. For the sake of brevity, only the $\beta = 15°$ and $\beta = 40°$ mixed-mode conditions are shown. The columns once again describe the approach utilized; the rows, however, separate the K_I and K_{II} values of each crack angle.

Table 5 Variation of SIF to crack tip location in DGS

Geometry	Approach	Standard Deviation (MPa$\sqrt{\text{m}}$)	RMSE (MPa$\sqrt{\text{m}}$)
$\beta = 15°$	Legacy K_I	0.125 0	0.0961
	Legacy K_{II}	0.0345	0.0197
	Combined K_I	0.106 0	0.0921
	Combined K_{II}	0.0713	0.0314
$\beta = 40°$	Legacy K_I	0.0780	0.0079
	Legacy K_{II}	0.0772	0.0051
	Combined K_I	0.0559	0.0039
	Combined K_{II}	0.0711	0.0059

As can be seen in Fig. 14, the legacy and new approaches perform similarly to the introduction of crack tip perturbations. It is prudent to note once again that even if $N < 3$ the combined fields method tends to perform more reliably, but if $N > 3$ both methods perform similarly. These results are further quantified in Table 5. The table lists each geometric condition as well as the standard deviation and RMSE of each approach. The standard deviation represents the average amount of deviation in the extracted data without regard to the predicted value, while the RMSE represents the average error the extracted value has relative to the predicted. For example, in the $\beta = 15°$ case, the standard deviation of K_I for the legacy approach is 0.1250 (MPa$\sqrt{\text{m}}$), and the RMSE is 0.0961 (MPa$\sqrt{\text{m}}$). These values are marginally higher than the ones for the combined field approach; standard deviation of 0.1060 (MPa$\sqrt{\text{m}}$) and an RMSE of 0.0921(MPa$\sqrt{\text{m}}$). However, the K_{II} standard deviation for the legacy approach is 0.0345 (MPa$\sqrt{\text{m}}$), and the RMSE is 0.0197 (MPa$\sqrt{\text{m}}$) whereas for the combined fields approach they increase marginally to 0.0713 (MPa$\sqrt{\text{m}}$), and the RMSE is 0.0314 (MPa$\sqrt{\text{m}}$), respectively. Similar observations can be made for $\beta = 40°$ case and others as well. Thus, it is reasonable to conclude that the two approaches perform similarly in terms of robustness to crack tip deviations.

In order to quantify the robustness of each method in regards to changes in the ROI, two additional distinct regions were selected to be contrasted against each other. The ROI is expressed in terms of the normalized radial extent r/B and angular extent θ relative to the local coordinates. In this analysis, only the former was changed from $0.3 < r/B < 1.2$ and $0.8 < r/B < 1.7$ and the results are shown in Fig. 15. Similar to the crack tip variation plots, the K_I and K_{II} values are separated across rows, and the columns describe each approach. Here, the red and blue series correspond to the two regions of interest.

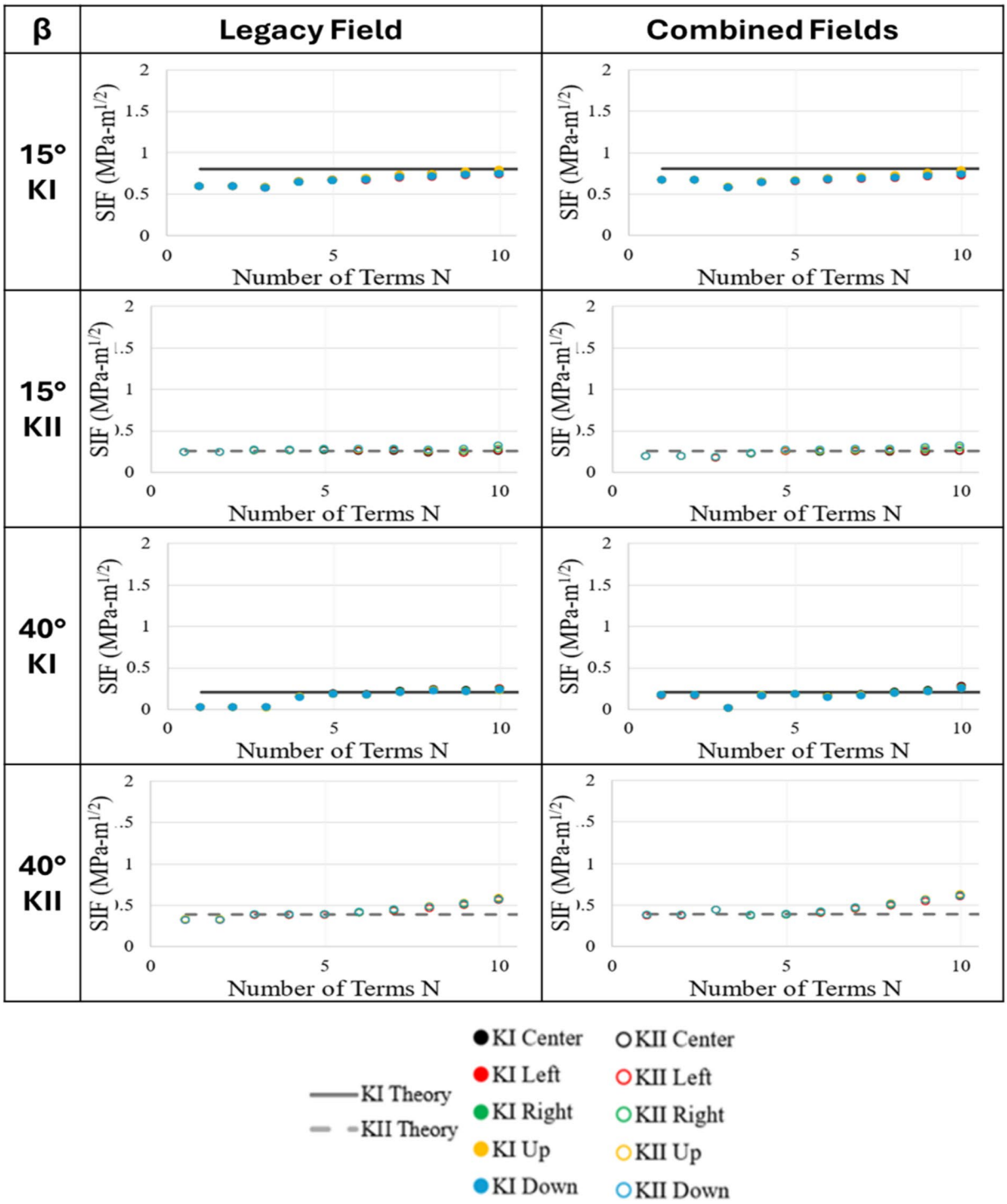

Fig. 14 Variation of SIFs due to different crack tip position selection in the legacy and combined fields approaches using DGS. (Legacy method uses ϕ_x field in the analysis)

In examining the data in Fig. 15, it can be observed that the combined fields approach shows improved robustness in comparison to the legacy approach. For example, in the row corresponding to the $\beta = 40°$ K_I extraction, it can be seen that the two data series are more consistent in the combined fields approach as opposed to the legacy approach. This is further quantified by the standard deviation and RMSE values in Table 6. The standard deviation

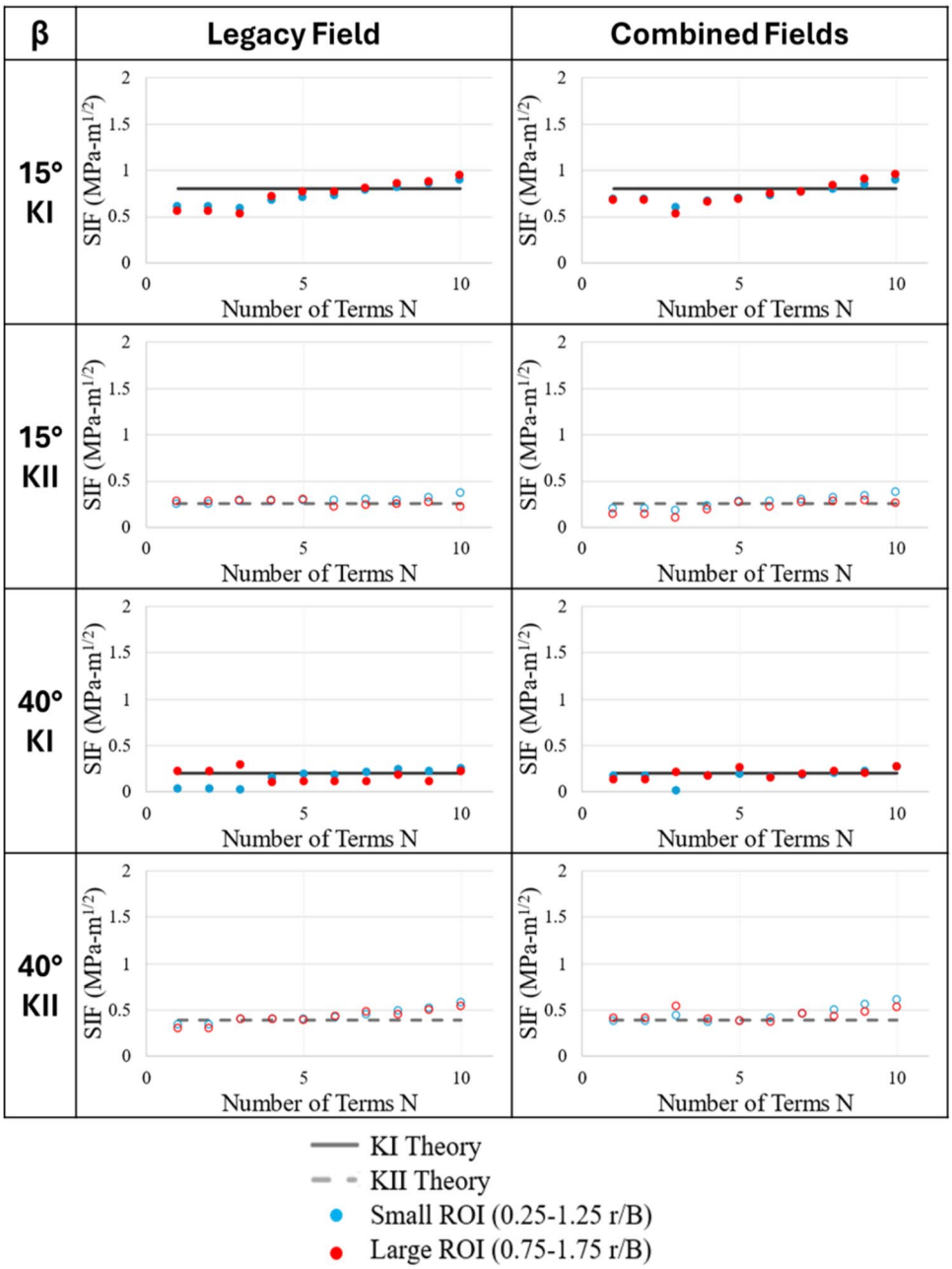

Fig. 15 Variation of SIFs for two different regions of interest for the legacy and combined fields approaches in DGS. (Legacy method uses ϕ_x field in the analysis)

and RMSE of the new approach are slightly better than that of the legacy approach, although the difference is small. For example, in the $\beta = 15°$ experiments, the legacy approach's standard deviation of extraction for K_I is 0.1194 (MPa$\sqrt{\text{m}}$), and in the combined fields approach the value is 0.0950 (MPa$\sqrt{\text{m}}$). The legacy K_I values have an RMSE of 0.0168 (MPa$\sqrt{\text{m}}$), whereas the combined field approach has an RMSE of 0.0132 (MPa$\sqrt{\text{m}}$). At the same time, the corresponding standard deviation for K_{II} increased marginally from 0.0393 (MPa$\sqrt{\text{m}}$) to 0.0485 (MPa$\sqrt{\text{m}}$) and RMSE from 0.002 (MPa$\sqrt{\text{m}}$) to 0.0023 (MPa$\sqrt{\text{m}}$). These differences can be seen in both crack geometries, where

Table 6 Robustness of SIFs to ROI selection in DGS

Geometry	Approach	Standard Deviation (MPa$\sqrt{\text{m}}$)	RMSE (MPa$\sqrt{\text{m}}$)
$\beta = 15°$	Legacy K_I	0.1184	0.0168
	Legacy K_{II}	0.0393	0.0020
	Combined K_I	0.0950	0.0132
	Combined K_{II}	0.0485	0.0023
$\beta = 40°$	Legacy K_I	0.1881	0.0375
	Legacy K_{II}	0.1654	0.0445
	Combined K_I	0.1412	0.0219
	Combined K_{II}	0.1572	0.0439

the combined fields method slightly outperforms the legacy approach, especially in the extraction of K_I.

Conclusions

In this work, extraction of SIFs from multiple orthogonal mechanical fields used in tandem is assessed relative to the legacy approach of selectively employing one of the measured fields. The over-deterministic least-squares error minimization of measured fields to extract SIFs are examined over a wide range of mixed-mode conditions from pure mode-I to mode-II. Two vision-based full-field optical methods DIC and DGS which measure two orthogonal fields simultaneously and are distinctly different in terms of the measured fields but rooted in the same speckle pattern correlation principle are investigated. The fields assessed are crack tip displacements and stress gradients in two orthogonal planar directions in semi-circular beam (SCB) geometries with five different crack angles. In all, the combined fields method results in a clear and consistent improvement over the legacy approach in both DIC and DGS. Furthermore, as the over-deterministic linear least-squares analysis is a post-processing step, the combined fields approach can be implemented for any prior data as long as data for both the fields has been preserved.

In DIC, the improvement in the accuracy and robustness of the method, and its ability to withstand potential operator errors in all mixed-mode cases is strongly evident. The number of higher order terms of the asymptotic crack tip field used in the analysis, the positional error of the crack tip by the operator, and the region of interest where the data are selected from, all have minor effect on the extracted value of SIF when using the combined fields approach. These improvements are especially clear for the mode-II SIF. Additionally, an order of magnitude reduction in the standard deviation and root mean squared error in the SIF values are quantified in the mixed-mode examples considered.

In DGS, as in DIC, using both the measured fields in tandem again offer greater consistency of determining accurate mixed-mode SIFs although the legacy method is shown to be quite comparable. This is attributed to the nature of DGS field that produces (a) larger angular deflections close to the crack unlike DIC where larger displacements occur at farther distances from the crack tip and (b) the absence of the constant T-stress term in the stress gradient fields. In terms of robustness, the combined fields method slightly outperforms the legacy method when crack-tip position or region of interest are varied. *Accordingly, it is always prudent to employ multiple available component fields in tandem for reliably extracting SIFs.*

Acknowledgements Partial support for this work under the US Army Research Office grant W911NF-22-1-0015 and National Science Foundation CMMI grant #2113948 are gratefully acknowledged.

Data Availability The datasets generated and analyzed during the current study are available from the authors upon request.

Declarations

Ethical Approval This article does not contain any studies with human participants or animals performed by any of the authors.

Conflicts of Interest The authors declare that they have no potential conflicts of interest.

References

1. Dondeti S, Tippur HV (2020) A comparative study of dynamic fracture of soda-lime glass using photoelasticity, digital image correlation and digital gradient sensing techniques. Exp Mech 60:217–233
2. Pfaff RD, Washabaugh PD, Knauss WG (1995) An interpretation of Twyman-Green interferograms from static and dynamic fracture experiments. Int J Solids Struct 32(6–7):939–955
3. Tippur HV, Chiang FP (1991) Analysis of combined moire and laser speckle grating methods used in 3-D crack tip deformation measurements. Appl Opt 30(19):2748–2756
4. Tippur HV (2010) Coherent gradient sensing (CGS) method for fracture mechanics: a review. Fatigue Fract Eng Mater Struct 33(12):832–858
5. Sanford RJ, Dally JW (1979) A general method for determining mixed-mode stress intensity factors from isochromatic fringe patterns. Eng Fract Mech 11(4):621–633
6. Sutton MA, Orteu JJ, Schreier H (2009) Image correlation for shape, motion and deformation measurements: basic concepts, theory and applications. Springer Science & Business Media
7. Periasamy C, Tippur HV (2012) Full-field digital gradient sensing method for evaluating stress gradients in transparent solids. Appl Opt 51(12):2088–2097
8. Kirugulige MS, Tippur HV (2009) Measurement of fracture parameters for a mixed-mode crack driven by stress waves using image correlation technique and high-speed digital photography. Strain 45(2):108–122
9. Harilal R, Vyasarayani CP, Ramji M (2015) A linear least squares approach for evaluation of crack tip stress field parameters using DIC. Opt Lasers Eng 75:95–102
10. McNeill SR, Peters WH, Sutton MA (1987) Estimation of stress intensity factor by digital image correlation. Eng Fract Mech 28(1):101–112
11. Méité M, Dubois F, Pop O, Absi J (2013) Mixed mode fracture properties characterization for wood by digital images correlation and finite element method coupling. Eng Fract Mech 105:86–100
12. Reddy MS, Ramesh K, Thiyagarajan A (2018) Evaluation of mode-I SIF, T-stress and J-integral using displacement data from digital image correlation–Revisited. Theoret Appl Fract Mech 96:146–159
13. Lammens B, Portemont G, Berthe J, Seghir R, Réthoré J (2024) Determining singular and non-singular Williams' expansion terms from full-field measurements: Consideration of structural effects on fracture behavior. Theoret Appl Fract Mech 1(130):104304

14. Torabi AR, Bahrami B, Ayatollahi MR (2019) Experimental determination of the notch stress intensity factor for sharp V-notched specimens by using the digital image correlation method. Theoret Appl Fract Mech 103:102244
15. Cappello R, Pitarresi G, Xavier J, Catalanotti G (2020) Experimental determination of mode I fracture parameters in orthotropic materials by means of Digital Image Correlation. Theoret Appl Fract Mech 108:102663
16. Kojouri AS, Rikaee HK, Kalteremidou KA, Van Hemelrijck D (2023) Experimental evaluation of J-integral in elastic and elastic–plastic polymers by means of digital image correlation and higher-order eigenfields under mode-I. Eng Fract Mech 291:109534
17. Beretta S, Patriarca L, Rabbolini S (2017) Stress Intensity Factor calculation from displacement fields. Frattura e Integrita Strutturale 11(41):269–276
18. Hao W, Tang C, Ma Y (2016) Study on crack-inclusion interaction using digital gradient sensing method. Mech Adv Mater Struct 23(8):845–52
19. Zhang R, He L (2012) Measurement of mixed-mode stress intensity factors using digital image correlation method. Opt Lasers Eng 50(7):1001–1007
20. Eshraghi I, Dehnavi MR, Soltani N (2014) Effect of subset parameters selection on the estimation of mode-I stress intensity factor in a cracked PMMA specimen using digital image correlation. Polym Testing 37:193–200
21. Mokhtarishirazabad M, Lopez-Crespo P, Moreno B, Lopez-Moreno A, Zanganeh M (2016) Evaluation of crack-tip fields from DIC data: A parametric study. Int J Fatigue 89:11–19
22. Yates JR, Zanganeh M, Tai YH (2010) Quantifying crack tip displacement fields with DIC. Eng Fract Mech 77(11):2063–2076
23. Tippur HV, Krishnaswamy S, Rosakis AJ (1991) A coherent gradient sensor for crack tip deformation measurements: analysis and experimental results. Int J Fract 48:193–204
24. Yoneyama S, Ogawa T, Kobayashi Y (2007) Evaluating mixed-mode stress intensity factors from full-field displacement fields obtained by optical methods. Eng Fract Mech 74(9):1399–1412
25. Kirugulige MS, Tippur HV, Denney TS (2007) Measurement of transient deformations using digital image correlation method and high-speed photography: application to dynamic fracture. Appl Opt 46(22):5083–5096
26. Isaac JP, Dondeti S, Tippur HV (2020) Crack initiation and growth in additively printed ABS: effect of print architecture studied using DIC. Addit Manuf 36:101536
27. Owens AT, Tippur HV (2021) Measurement of mixed-mode fracture characteristics of an epoxy-based adhesive using a hybrid digital image correlation (DIC) and finite elements (FE) approach. Opt Lasers Eng 140:106544
28. Chong KP, Kuruppu MD (1984) New specimen for fracture toughness determination for rock and other materials. Int J Fract 26(2):R59-62
29. Ayatollahi MR, Aliha MR, Hassani MM (2006) Mixed mode brittle fracture in PMMA - An experimental study using SCB specimens. Mater Sci Eng, A 417(1–2):348–356
30. Fahem A, Kidane A, Sutton M (2021) Loading Rate Effects for Flaws Undergoing Mixed-Mode I/III Fracture. Exp Mech 61(8):1291–1307
31. Owens AT, Tippur HV (2023) An image processing technique to identify crack tip position and automate fracture parameter extraction using DIC: application to dynamic fracture. Exp Mech 63(3):445–466
32. Xie Y, Cao P, Jin J, Wang M (2017) Mixed mode fracture analysis of semi-circular bend (SCB) specimen: A numerical study based on extended finite element method. Comput Geotech 82:157–172
33. Pan B (2018) Digital image correlation for surface deformation measurement: Historical developments, recent advances and future goals. Meas Sci Technol 29(8):082001
34. Becker TH (2024) Extracting fracture properties from digital image and volume correlation displacement data: A review. Strain 60(4):e12469
35. Periasamy C, Tippur HV (2013) Measurement of orthogonal stress gradients due to impact load on a transparent sheet using digital gradient sensing method. Exp Mech 53:97–111
36. Sundaram BM, Tippur HV (2016) Dynamic crack growth normal to an interface in bi-layered materials: an experimental study using digital gradient sensing technique. Exp Mech 56:37–57